Winter 1-31-2024

# Nanostructured Cu-Zn Electrode Materials for Green Hydrogen Production

Rahma Leil
rahma.a.leil@aucegypt.edu

;/

The American University in Cairo
الجامعة الأمريكية بالقاهرة

Graduate Studies

# *Nanostructured Cu-Zn Electrode Materials for Green Hydrogen Production*

A THESIS SUBMITTED BY

Rahma Leil

TO THE

*Nanotechnology Program*

[Date]

*in partial fulfillment of the requirements for the degree of*

*Masters of Science in Nanotechnology*

# Declaration of Authorship

I, Rahma Leil , declare that this thesis titled, “Nanostructured Cu-Zn Electrode Materials for Green Hydrogen Production” and the work presented in it are my own. I confirm that:

- This work was done wholly or mainly while in candidature for a research degree at this University.
- Where any part of this thesis has previously been submitted for a degree or any other qualification at this University or any other institution, this has been clearly stated.
- Where I have consulted the published work of others, this is always clearly attributed.
- Where I have quoted from the work of others, the source is always given. With the exception of such quotations, this thesis is entirely my own work.
- I have acknowledged all main sources of help.
- Where the thesis is based on work done by myself jointly with others, I have made clear exactly what was done by others and what I have contributed myself.

Signed:

_____

Date:

_____

# Abstract

The continuity of human civilization heavily depends on securing sources of energy. After the 1970s energy crisis, scientists and engineers are meticulously looking for fuels that are alternatives to fossil fuels. Hydrogen can store solar energy to be further used as a fuel. One of the renewable ways to produce hydrogen is Photoelectrochemical (PEC) water splitting. PEC water splitting is a promising way to produce green hydrogen. However, one of the bottlenecks in realizing scalable green hydrogen production systems is the inability to identify and fabricate earth-abundant, stable, and durable photocathodes. The main challenges with the reported photocathodes so far are their instability in aqueous solutions and the use of precious unabundant materials. To this end, the use of scrap materials to fabricate highly stable photocathodes would solve the two main challenges. Herein, scrap brass alloys with different zinc contents were used to fabricate photocathodes for photoelectrochemical green hydrogen production. The scrap brass alloy with 5% Zn showed enhancement in the photocurrent density of -0.26 mA/cm$^2$ at 0.62 V vs reversible hydrogen electrode (RHE) , high long-term stability up to four hours under continuous illumination, high charge carrier density of $6.2\times10^{21}$ cm$^{-3}$ and less total resistance than the other brass samples. Through electrochemical impedance spectroscopy (EIS), the presence of surface states was verified. The 95Cu-5Zn sample showed an amount of evolved hydrogen of 0.2658 µmole after one hour of continuous illumination, while the 100Cu sample only showed 3.965 nmole after 20 minutes of continuous illumination before being completely reduced to copper. Density functional theory calculations were used to study the optical and electronic properties of the best-performing sample. This work is the first to systematically and fundamentally study scrap brass as a promising material for a more stable and durable PEC water splitting.

# Acknowledgments

I would like to express my deepest gratitude to my supervisor, Dr. Nageh Allam, for being such a supportive mentor in all aspects. He is so knowledgeable that I have never talked to him without gaining valuable insights. His guidance, patience with slow progress, comments, and suggestions throughout the thesis work made me encouraged to be self-motivated, and self-disciplined, and pointed me to the right track.

My gratitude goes to Dr. Deirdre O'Carroll for hosting me in her lab to do further experiments that were necessary for the completion of this work. I am also thankful to Dr. Ehab Elsawy for his time and insightful discussions regarding electrochemistry. I also thank the examination committee for taking the time to review my work.

My gratitude also goes to all members of the Energy Materials Laboratory (EML). Thanks to the initial training and support of Nashaat Ahmed, Mohamed Ramadan, and Eslam Mamdouh, I was able to conduct electrochemical experiments. I also appreciate all the valuable discussions I had with all the members of EML during group meetings, and all the sincere help from all the members, especially Ibrahim Badawy, Dr. Basamat Shaheen, Dr. Menna Hassan, Dr. Doha Sayed, Dr. Ghada Khedr, Dr. Manar Hazaa, Mohamed Mahrous, Aya Kamal, Loujain Gamal, Sara Teama, Yasmine Ibrahim, and Nada Tarek. The support from EML members was not only academic and work-related, but it was also valuable in terms of all the friendships I made that helped me get out of the tough times.

Finally, I would like to thank all my professors at the AUC for their teaching and guidance, and I would like to acknowledge the financial support by the AUC through my study abroad program, and the research grant I have received.

# Dedication

This thesis is dedicated to my mother, Marwa, my father, Ahmed, my sister, Raneem, and my brother, Mohamed.

# Table of Contents

# List of Figures

# List of Abbreviations

| | |
|---|---|
| PEC | Photoelectrochemical |
| SCL | Space Charge Layer |
| $E_{vac}$ | Vacuum level, |
| $E_{CB}$ | Bottom of the conduction band |
| $E_{VB}$ | Top of the valence band |
| IE | Ionization energy |
| XRD | X-Ray Diffraction |
| XPS | X-Ray Photoelectron Spectroscopy |
| UPS | Ultraviolet Photoelectron Spectroscopy |
| EBS | Electronic Band Structure |
| PDOS | Partial Density of States |
| OCV | Open Circuit Voltage |
| CV | Cyclic Voltammetry |
| LSV | Linear Sweep Voltammetry |
| CA | Chronoamperometry |
| EIS | Electrochemical Impedance Spectroscopy |
| RHE | Reversible Hydrogen Electrode |
| EC | Equivalent Circuit |
| M-S | Mott-Schottky |
| OER | Oxygen Evolution Reaction |
| HER | Hydrogen Evolution Reaction |

# List of Symbols

| | |
|---|---|
| $V_B$ | Magnitude of band bending |
| X | Electron affinity |
| Φ | Work function |
| $W_d$ | Width of Space Charge Layer |
| $\boldsymbol{\lambda_D}$ | Debye length |
| U | Applied potential |
| $\boldsymbol{U_{f_b}}$ | Flatband potential |
| k | Boltzmann constant, |
| T | Absolute temperature. |
| $\boldsymbol{\varepsilon_r}$ | Relative permittivity |
| $\boldsymbol{\varepsilon_0}$ | Permittivity of free space |
| $\boldsymbol{N_D}$ | Charge carrier concentration |
| e | Elementary charge |
| C | Capacitance |
| A | Surface Area |
| β | Half-width at half maximum |
| ε | Lattice strain |
| θ | Bragg angle |
| d | Average crystallite size |
| λ | wavelength of the x-ray |
| $\tau_A$ | Decay time due to the harmonic process |
| $\tau_l$ | Decay time due to the impurities present |

| | |
|---|---|
| $\hbar$ | Reduced Planck constant |
| $\Delta E$ | Uncertainty in the phonon mode energy |
| c | Velocity of light |
| $\Gamma$ | Full width at half maximum |
| $\chi$ | Electron affinity |
| $h\nu$ | Excitation energy |
| $w$ | Constant in UPS |
| $E_g$ | Bandgap |
| $I_t$ | Current at time (t) |

# Chapter 1

# Introduction

## 1.1 Energy Crisis

The continuity of human civilization heavily depends on securing sources of energy. In fact, energy security has been a significant point of research since the 1970s amid the oil crisis. Many wars occurred for the sake of reserving sources of energy. For instance, the Bush administration decided to invade Iraq in 2003 for its crude oil reserves [1]. The energy crisis came back after the COVID-19 pandemic, and the crisis has taken a sharper turn after the Russia-Ukraine conflict that affected everyday household costs for energy used in heating, cooling, and other everyday usage of energy [2]. Energy plays an important role in several sectors such as business, industry, healthcare, education, agriculture, national defense, and almost all services sectors. Energy plays an important role in determining whether the country is a developed country or a developing country, and it is a reason for social uplift. The lack of energy resources in Egypt has adversely affected the industrial sector, led to the minimization of exports due to the unaffordable costs of production, increased the prices of essential goods, increased the unemployment rates, and led many international businesses to close in Egypt [3]. The crisis in Egypt has been exacerbated especially after the government announced a reducing electricity load plan that includes power cuts that last from one hour to two hours every day.

The world mainly depends on fossil fuels as a source of energy. For instance, more than

80% of the world's energy is supplied by fossil fuels ( 30.95% from oil, 24.42% from natural gas, and 26.9% from coal) [4] , as shown in **Figure *1.1*** . Therefore, the energy crisis does not stop at the previously illustrated points, the problem includes that the current sources of energy are an environmental hazard due to the emission of carbon dioxide, which is the main cause of global warming resulting in climate change and air quality concerns. In 2021, more than 34 billion tons of carbon dioxide were emitted to the environment, as a direct consequence of fossil fuel consumption[5]. In May 2023, atmospheric carbon dioxide hit 424 ppm, which represents a 10% increase since 2005, when the atmospheric carbon dioxide hit 379.1 ppm and it is 50% higher than the amount it was before the industrial revolution [6]. Counterintuitively, developed countries consume more energy and contribute more to global carbon emissions causing energy inequity in the world, while developing countries contribute to the reduction of the global carbon emission [7]. The increase in carbon dioxide amounts will lead to the increase of Earth's temperature affecting human health, and crop yields, the destruction of coastal and small island communities, and the imbalance of many ecosystems endangering many species of plants, animals, and marine life. An interesting study using Artificial Neural Networks (ANN) indicates that even with substantial effort for the mitigation of greenhouse gases, there is still a possibility of failing to hold global warming below the 2°C threshold, meaning that we will reach global warming threshold by mid-century [8]. Moreover, the world is expected to suffer from fossil fuel shortage shortly, meaning that the energy crisis will be more severe leading to affecting all the service sectors mentioned above and the fossil fuel will

no longer be able to meet the increasing energy demands.

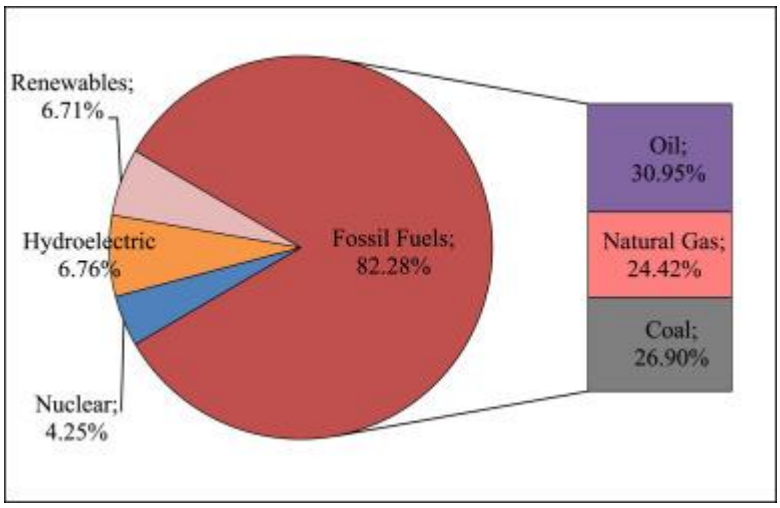


**Figure 1.1** The World's sources of energy by type of fuel [4].

To meet the energy demands of billions of people in the world, Professor Rick Smalley, a Nobel laureate in 1996 for the discovery of $C_{60}$, asserted that the world needs to transform into renewable sources of energy independent of carbon emission. Therefore, scientists and researchers pursue renewable energy sources.

## 1.2 Renewable Sources of Energy

As mentioned previously, clean energy sources are the ultimate choice to meet the increasing energy demand. Due to the increase in awareness about the risks of dependence on fossil fuels, many researchers and decision-makers shifted towards the usage of renewable energy. An official report by the International Energy Agency (IEA) states that the global demand for fossil fuels has decreased since 2019, while there is a noticeable increase in the usage of renewable energy sources, as shown in **Figure 1.2** [9]. Different renewable energy sources have been introduced to the market and in research recently, such as wind power, hydropower, solar energy, bioenergy, geothermal energy, and hydrogen energy.

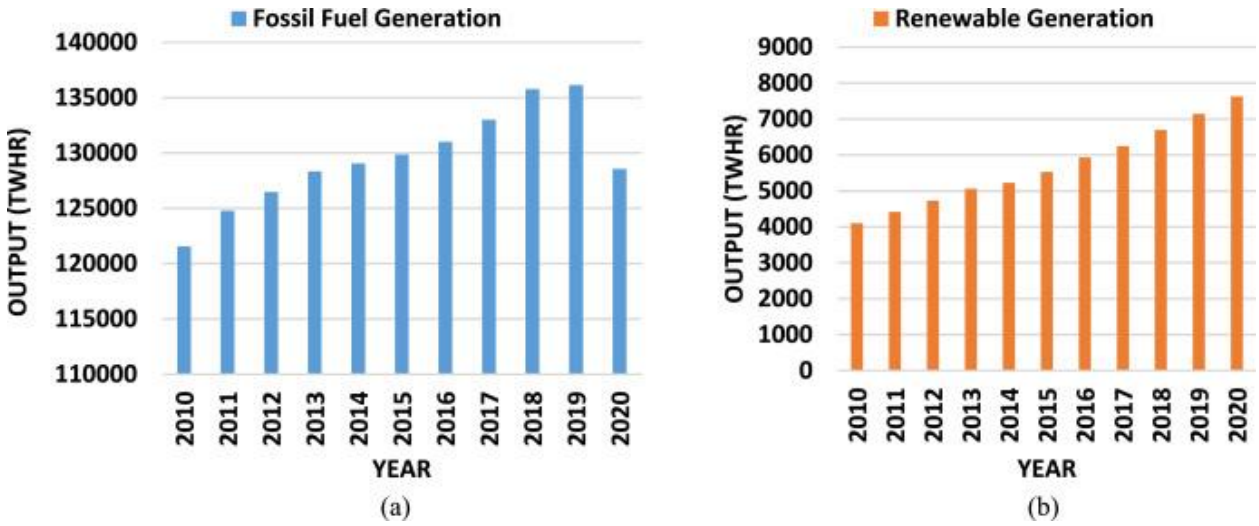


**Figure 1.2** (a) The decline in the usage of fossil fuel, and (b) The increase in the usage of renewable energy sources [9].

## 1.3 Hydrogen Energy

In 1766, hydrogen was discovered by Henry Cavendish. In 1787, Antoine Lavoisier named this new gas "Hydrogen". Hydro and genes mean water former. Hydrogen has many uses in our everyday life. It can be used in ammonia synthesis, which is a very important industry to produce fertilizers. In addition, hydrogen can be used as a fuel in transportation and to generate electricity in fuel cells. Thus, looking for sources to produce hydrogen is of paramount importance. The simplest atom is the hydrogen atom consisting of one proton and one electron; therefore, the hydrogen atom is very reactive preferring to exist in the molecular form ($H_2$). Hydrogen energy is a non-toxic and clean energy source; however, hydrogen is not a primary source of energy. Indeed, there is a required energy to extract hydrogen from its sources. The energy content of 9.5g of hydrogen is equivalent to 25 g of gasoline. Hydrogen

could be stored for the generation of electricity for a period of time. Moreover, the by-product of hydrogen energy, when used in a fuel cell, is water vapor, which is harmless to the environment. There are many methods to generate hydrogen energy, some of which are non-renewable, and others are renewable. Most of the world's production of hydrogen, 80%, comes from steam methane reforming at an efficiency of 85%. However, the reforming of methane is neither green nor sustainable. Moreover, the quality of the produced hydrogen is very low because C, S, and N oxides are also obtained as by-products. Thus, there must be a search for alternative sources of hydrogen. Hydrogen can only be considered as a green fuel, if the source of the hydrogen is renewable, such as solar power, wind power, and hydroelectric power. Hydrogen can be renewably produced by electrolysis, biohydrogen, thermochemical cycles, photocatalysis, and plasmolysis. Among the several ways to produce hydrogen, electrolysis has an efficiency of 52%. In addition, the cost of electrolysis is $ 10.3/kg. Therefore, the process has many challenges in terms of its cost, and efficiency[10]. Another option that needs to be taken into account is photoelectrochemical (PEC) water splitting to produce green hydrogen. According to the US Department of Energy (DoE), the ultimate target for photoelectrochemical hydrogen cost is $2/kg, so that the process can be competitive with other processes to produce hydrogen. In addition, the solar to hydrogen efficiency must exceed 10%[11].

### 1.3.1 Solar Energy and Hydrogen Generation

Considering renewable energy sources, solar energy can be thought of as the future of the world to meet the increasing energy demand of the increasing population for several reasons. The first reason is that solar energy is the most abundant source of energy, as the sun emits at a rate of $3.8 \times 10^{23}$ kW. Out of that huge number, $1.8 \times 10^{14}$ kW are dissipated by the earth. As the sun is burning on a nuclear fusion reaction releasing energy, the energy of the

sun reaches earth in various forms, such as heat and light. Some of the energy is lost due to absorption, scattering, and reflection by clouds. The second reason is that solar energy is not exhaustible. Fortunately, Egypt was given solar energy due to its location; the average solar radiation in Egypt is 8.1 kWh/$m^2$/day. The third reason for the superiority of solar energy is that its use does not harm the environment [12].

### 1.3.2 Generation of Hydrogen by Water Splitting

Nowadays, it has become obvious that water is the future of hydrogen generation. However, some critics ask the question of whether there is enough water to support the hydrogen economy. Some scientists and researchers argue that the answer is No due to the increasing water demand. To meet the energy demands using hydrogen energy, 2.3 Gt of hydrogen are needed. According to the reaction stoichiometry, for every 1 kg of hydrogen produced, 9kg of water must be consumed. Thus, 2.3 Gt of hydrogen requires 20.5 billion $m^3$ of fresh water, which accounts for 1.5 ppm of Earth's available freshwater resources. Moreover, many researchers are focusing on hydrogen extraction from seawater, which will make the process more feasible and economically viable. Indeed, it is quite surprising that 31 billion $m^3$ of water were consumed for power generation and energy production from fossil fuels, using this amount of water for cooling, mining, hydraulic fracturing, and refining. It is a fair statement that 20.5 billion $m^3$ of fresh water is a lot to be withdrawn for hydrogen production. However, this is still 33% less than what is consumed currently for fossil fuels related usage, as shown in **Figure 1.3** [13].

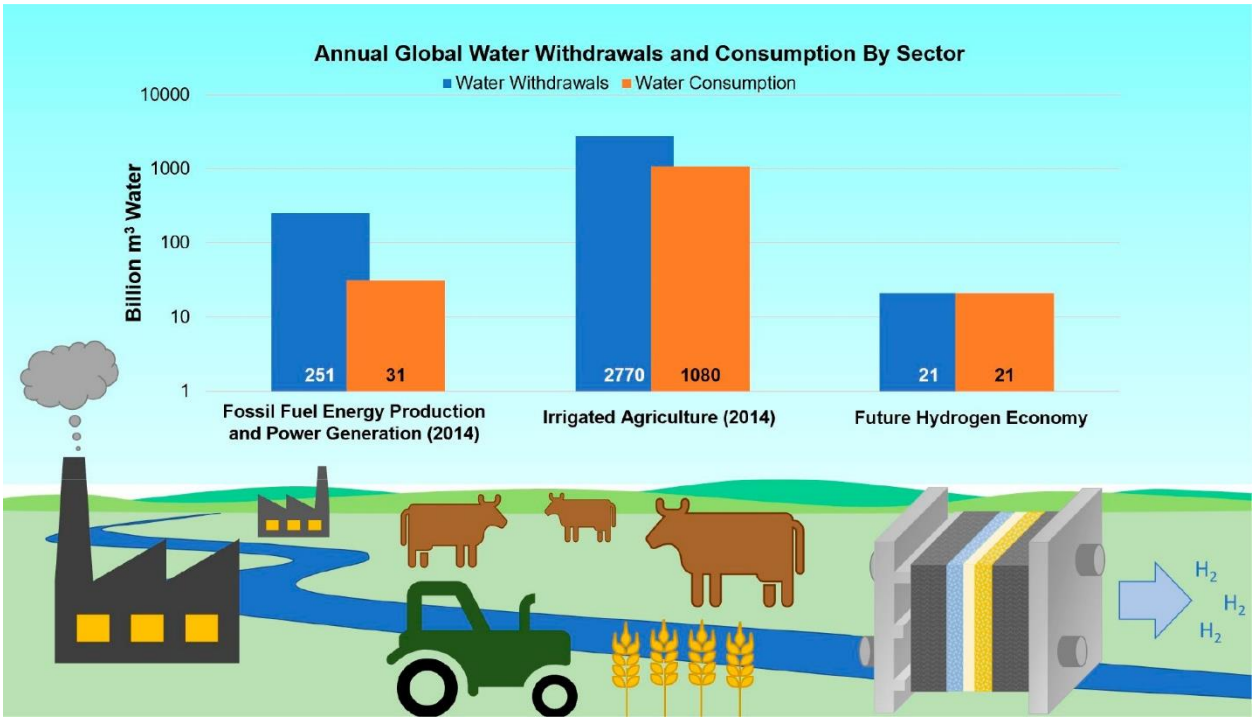


**Figure 1.3** Comparison of global freshwater withdrawal and consumption in three different sectors; fossil fuel energy production, irrigation, and future hydrogen economy [13].

There are several pathways through which hydrogen can be produced from solar energy. The first method is that solar energy can be used directly to heat water decomposing it into its components; in a process called thermolysis. The second way is that electricity can be generated using solar energy, then the resulting electricity can be used to produce hydrogen; in a process called electrolysis. The third method is that solar energy can be used directly to split water; in a process called photolysis.

## 1.4 Photoelectrochemical Water Splitting

After the analysis of the information mentioned in the preceding sections, it can be stated that the combination of the water electrolyzers with the sun power will be an optimized approach to reach maximum efficiency of water splitting, avoiding the costs of producing electricity. Plants make their food via natural photosynthesis. This was inspiring to researchers and scientists to introduce a biomimetic photo-assisted electrochemical system ( artificial photosynthesis). Although the solar spectrum contains the required energy to split water; the reaction is not spontaneous; due to the low absorption coefficient of water in the UV-visible region [14]. There is a need for the usage of semiconductor materials working as photoabsorbers for the water splitting in the electrochemical cell. There are several requirements for the semiconductor materials to be used as will be discussed later in this thesis. Moreover, hydrogen is strongly bonded to oxygen in the water molecule; therefore, a minimum energy of 1.229 eV is required for splitting water into oxygen and hydrogen.

In 1972, Honda and Fujishima were the first to use $TiO_2$ (an n-type semiconductor photoabsorber) as an anode, and Pt as a cathode in an aqueous electrolyte to split water; remarking that as the first time a photoelectrochemical cell was set up. In this setup, the solar radiation absorbed by $TiO_2$ results in oxygen evolution at the anode, and hydrogen evolution at the cathode. When using a p-type semiconductor, the same scenario goes on; taking into consideration that the illuminated part of the cell will be the cathode, not the anode. The setup of the PEC cell is shown in **Figure 1.4**.

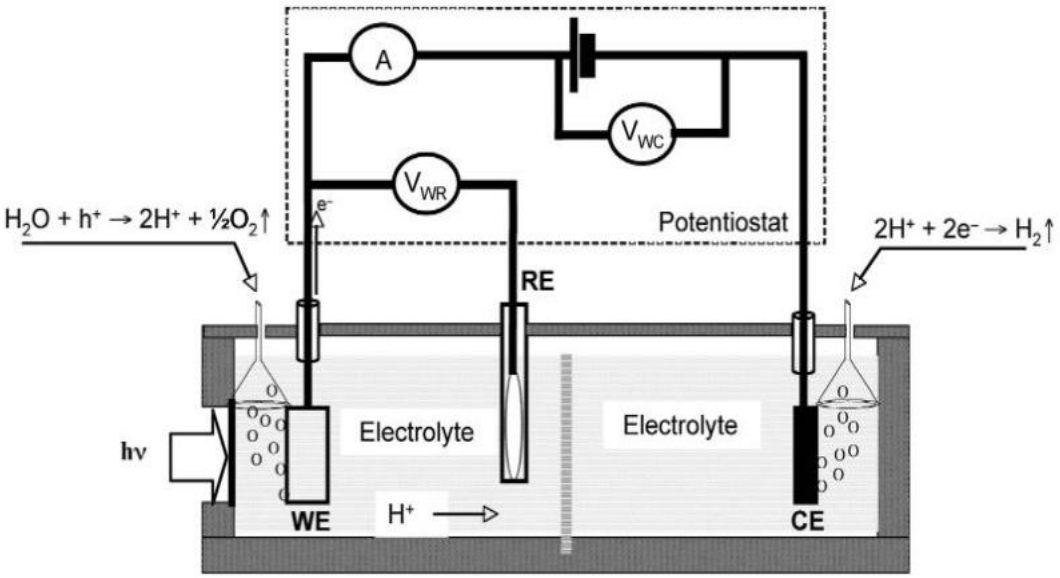


**Figure 1.4** Schematic diagram of a conventional three-electrode photoelectrochemical cell; showing working electrode (WE), reference electrode (RE), and counter electrode (CE)[15].

Even though $TiO_2$ showed higher stability than other semiconductors in PEC cells, it showed a very low efficiency of 0.1%. Even though the efficiency is low, the work of Fujishima and Honda was eye-opening to many researchers and scientists to further develop photoanodic and photocathodic materials for PEC. Thus, the current endeavors aim at designing and fabricating robust, earth-abundant, and efficient nanostructured materials for the anode and the cathode of a PEC cell.

In conclusion, constructing nanostructured semiconductors is of great importance to the development of PEC tandem cells. This thesis is one of the many trials.

## 1.5 Thesis Scope and Organization

This research work aims to achieve a performing photoelectrochemical water

splitting system by developing light-harvesting photocathodic materials**.** This thesis demonstrates the feasibility of achieving this aim by rationalizing the design of novel, nonprecious, durable, and active nanostructured photocathodes for hydrogen fuel production using cost-effective brass alloys. It will be explained in chapter 2 that the mechanism of a PEC cell relies on two factors:

(1) Maximizing light absorption by the choice of a suitable bandgap among the presented materials.

(2) Maximizing the charge carrier separation and promoting fast charge transport to the electrolyte.

In semiconductors, the two processes are competing. Thus, a balance between the two processes needs to be reached. To reach that balance, four concentrations of Zn alloying to Cu were systematically studied: 95Cu-5Zn, 85Cu-15Zn, 70Cu-30Zn, and 50Cu-50Zn. Then, the studied structures were compared to CuO nanostructures. The properties of the best-performing sample were studied using density functional theory (DFT).

**Chapter 2.** provides the scientific background regarding PEC water splitting; illustrating the terminologies used throughout that thesis, such as solar radiation, water splitting, photoelectrochemical water splitting, and semiconductors usage in photoelectrolysis.

**Chapter 3.** gives a literature review regarding the usage of CuO and brass alloy in PEC.

**Chapter 4.** provides a detailed description of the experimental procedures, computational methods, and characterization techniques used throughout the thesis.

**Chapter 5.** presents the results of the characterization techniques used to characterize the resulting semiconducting samples throughout the thesis.

**Chapter 6.** shows the results and the discussion concerning CuO and brass alloys in terms of their photoelectrochemical performance.

**Chapter 7.** highlights the conclusion of the study suggesting a plan for future work.

# Chapter 2

# Scientific Background

In this chapter, a fundamental scientific background is presented. The scientific background is regarding solar radiation, the interaction between the semiconductor and the electrolyte called semiconductor-electrolyte interface (SEI), photoelectrochemical water splitting, efficiency of photoelectrolysis, materials requirements for photoelectrolysis, corrosion and photocorrosion resistance, and losses in photoconversion processes.

## 2.1 Solar Radiation

Solar radiation is a result of the nuclear fusion reactions that occur inside the sun. Solar irradiance is the electromagnetic power the earth receives from the sun per unit surface area ($kW/m^2$). Solar radiation ($kWh/m^2$) represents the energy the earth receives per unit area. The solar radiation consists of different wavelengths, as displayed in **Figure 2.*1*** . The total irradiance for the spectrum of the sun, in the wavelength range of 0.3-0.4 µm, is reported to be 963 $W/m^2$. However, it can be normalized to 1000 $W/m^2$ because of the atmospheric variation, such as cloudness, dust, and humidity. (1000 $W/m^2$ is reported as 1 sun).

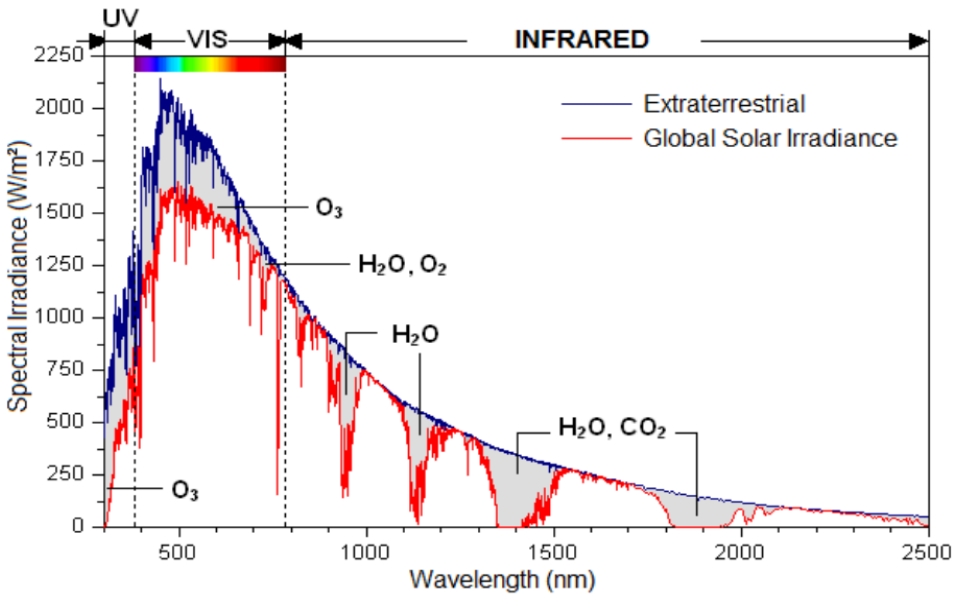


**Figure 2.1** Standard solar radiation spectrum [15].

The intensity of the solar radiation that reaches the earth depends on several factors, such as the geographical coordinates, the time of the year, the position of the sun, and the meteorological conditions. The figure shows a representative solar spectrum under the global AM 1.5 ( air mass 1.5) condition, which corresponds to a situation when the sum is at a Zenith angle of 48.19º (AM= [ 1/cos(48.19)]=1.5). Through this situation, we can conclude that the light travels through the atmosphere 1.5 times the distance it travels when the sun is at 0º Zenith angle. The concept of the Zenith angle is illustrated in **Figure 2.2**.

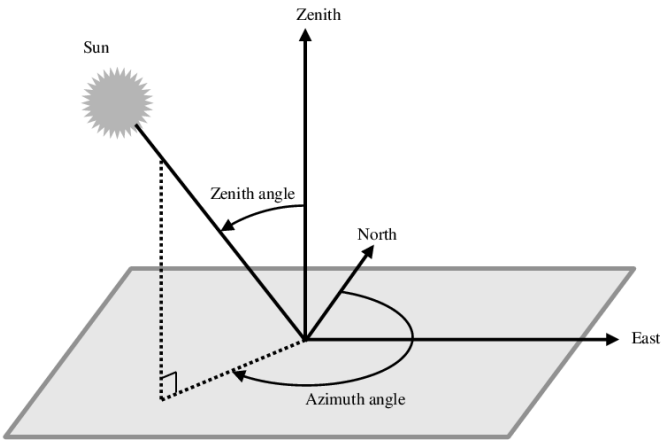


**Figure 2.2** Configuration for AM 1.5 solar irradiation[16].

## 2.2 Semiconductor-electrolyte interface

Before tackling the semiconductor-electrolyte interface, it is important to come across the concept of semiconductors and the concept of an electrolyte. Electronic states are delocalized in a perfect semiconductor, however, the current-carrying bands do not overlap as in metals, they are separated by the bandgap. The Fermi level is the level, where the probability of finding an electron is ½. Therefore, the Fermi level is closer to the conduction band, in the case of an n-type semiconductor and closer to the valence band in the case of a p-type semiconductor.

When a semiconductor is brought into contact with an electrolyte, a potential difference is established at the interface and the electrons will flow between the semiconductor and the electrolyte till equilibrium is established. After establishing equilibrium, the Fermi level is the same everywhere causing the formation of a space charge layer (SCL) associated with an upward band bending of the band edges (of magnitude $V_B$) in the case of an n-type semiconductor, and a downward band bending in the case of p-type semiconductor, as illustrated in **Figure 2.3**. Under dark conditions, the free space charge in the semiconductor side can exchange carriers with the redox pair, while the current drastically increases under illumination due to the increase in the minority charge carriers. It is worth noting that the

preceding discussion is mainly for ideal semiconductors without the presence of surface states [16,17].

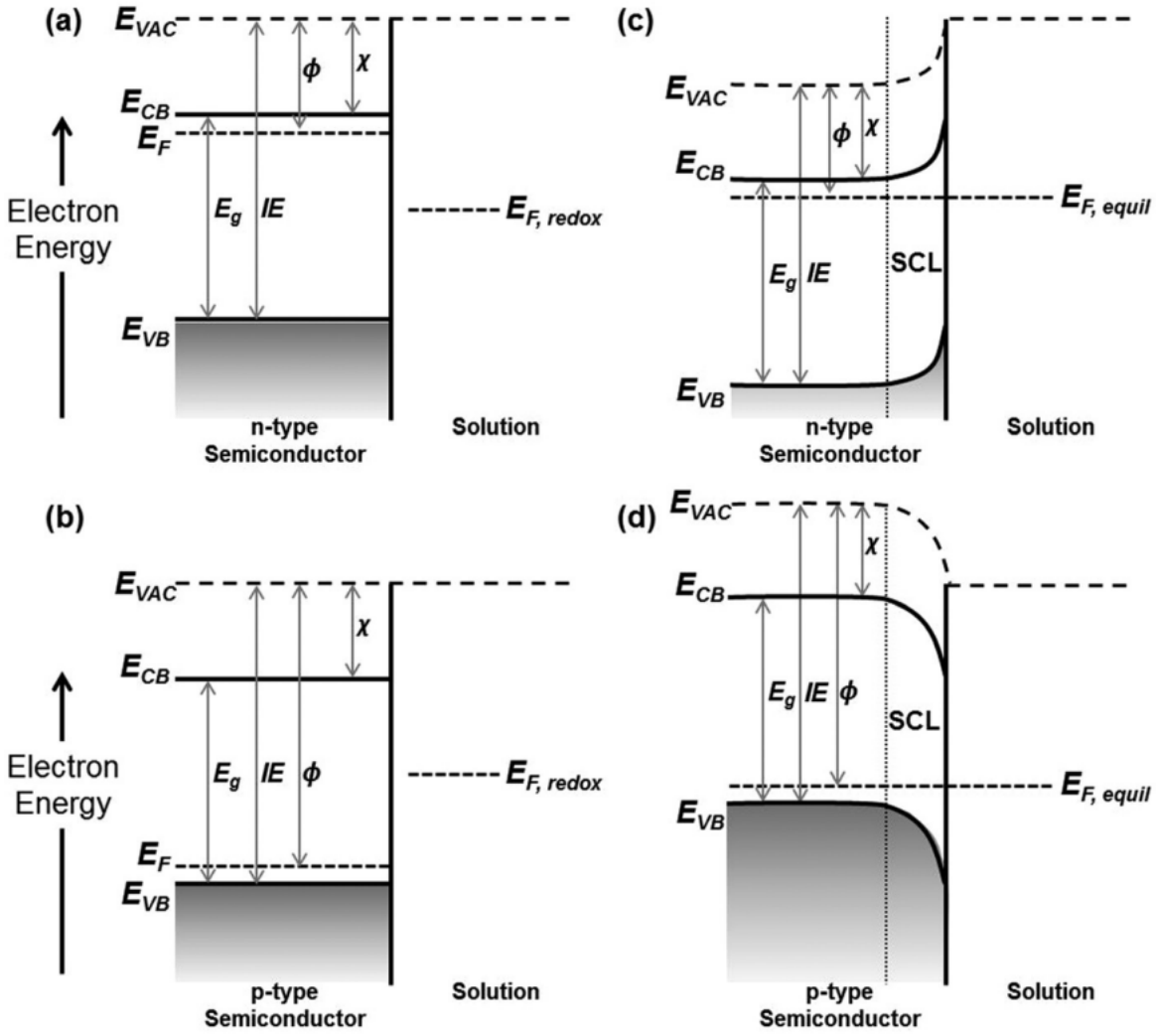


**Figure 2.3** Band structure of the semiconductor-electrolyte interface before contact for n-type and p-type semiconductors (a&b), while (c&d) show the direct contact under equilibrium for n-type and p-type semiconductors. $E_{vac}$: vacuum level, $E_{CB}$ : bottom of the conduction band, $E_{VB}$: top of the valence band, IE: Ionization energy, $\chi$: electron affinity, and $\Phi$: work function[17] .

It is worth mentioning that the charge transfer across the semiconductor-electrolyte

interface is a sluggish process due to the possible recombination between charge carriers. In case of no recombination, the theoretical onset potential should rise early. In reality, the practical onset potential shifts anodically or cathodically. This process is especially true for sluggish reactions such as water oxidation. The equilibration of the electrochemical potentials at the semiconductor-electrolyte interface leads to band bending of magnitude $V_B$. The space charge layer or the " depletion layer" has a width, which is represented by:

$$\boldsymbol{w_d = \lambda_D \left( \frac{2e|U - U_{f_b}|}{kT} - 1 \right)^{\frac{1}{2}}} \tag{2.1}$$

where $\boldsymbol{\lambda_D}$ is the Debye length (explained in the equation below), the distance over which charge separation can take place. U is the applied voltage, $\boldsymbol{U_{f_b}}$ is the flatband potential, k is Boltzmann constant, ant T is the absolute temperature.

$$\boldsymbol{\lambda_D = \left( \frac{\varepsilon_r \varepsilon_0 kT}{N_D e^2} \right)^{\frac{1}{2}}} \tag{2.2}$$

where $\boldsymbol{\varepsilon_r}$ is the relative permittivity, $\boldsymbol{\varepsilon_0}$ is the permittivity of free space, $\boldsymbol{N_D}$ is the charge carrier concentration, and e is the elementary charge.

The capacitance ( C ) per unit area (A) of the space charge layer can be obtained using the following equation:

$$\boldsymbol{\frac{C}{A} = \frac{\varepsilon_r \varepsilon_0}{w_d}} \tag{2.3}$$

Through the substitution of equation (2.1) in equation (2.3), we get the famous well-established *Mott-Schottky* equation:

$$\boldsymbol{\left(\frac{A}{C}\right)^2 = \frac{2}{eN_D \varepsilon_r \varepsilon_0} \left( \left| U - U_{f_b} \right| - \frac{kT}{e} \right)} \tag{2.4}$$

where A is the surface area of the electrode. When plotting $\boldsymbol{\left(\frac{A}{C}\right)^2}$ as a function of the applied

potential, this will give a straight line; through which we can determine the charge carrier concentration from the slope, and the flatband potential from the intercept.

At this stage of the thesis, we can explain what is meant by the flatband potential. The magnitude and direction of band bending can be adjusted by an externally applied potential, flatband potential is the applied bias that diminishes the band bending[18].

One can change the SCL by altering the potential of the semiconductor electrode with a potentiostat. Fermi level is elevated or lowered depending on the applied potential meaning that the whole band structure goes up or down depending on the applied potential. In this thesis, we will limit our discussion to the p-type semiconductor. For a p-type electrode, when $E < E_{fb}$ , the band bending collects the holes towards the bulk, and electrons are derived towards the surface and a depletion layer exists. A p-type semiconductor can produce photocurrent when it is irradiated, and it has a depletion layer. In this case, the electric field of the space charge layer separates the generated electron-hole pair; meaning that the electrons and holes will not recombine [19].

Through the previous discussion, we can conclude that the dark conditions are not favorable to photoelectrochemical water splitting due to the impossible to measure current due to the recombinations. However, the situation is different under illumination as charge carriers are generated, and then separated by the electric field in the space charge layer. In the case of a p-type semiconductor, the holes move into the bulk, and electrons migrate to the electrolyte interface resulting in a photovoltage, and the Fermi level is moved upwards to the flatband potential. Then, band bending is reduced. Under the aforementioned conditions, no current is flowing. Therefore , an overpotential needs to be applied for the current to flow; overpotential is the energy required to drive the reaction. The total overpotential is the sum of the overpotential across the depletion region and the Helmholtz layer. In concentrated solutions,

the voltage drop across the solution can be assumed to be small, leading to ignoring it in most cases. The interfacial activation energies for electron and hole transfer are related to the overpotentials. Under illumination conditions, the maximum Fermi level is the flatband potential, which is still below the hydrogen evolution potential, making the hydrogen evolution reaction impossible. When a bias is applied, the Fermi level is raised above the hydrogen reduction potential, allowing the reaction to occur.

If the photoelectrochemical process needs a large applied bias, this leads to lowering the efficiency of the process. Therefore the choice of the semiconductor material is of paramount importance to increase the efficiency of the water-splitting process. The next step in the thesis is to deeply introduce the concept of photoelectrochemical water splitting, how it occurs, the limitations of the process, and how to improve the efficiency of the process. As a general guideline, a successful PEC process depends on several factors mainly:

(1) Absorption of photons to generate electron-hole pairs.

(2) Charge separation in the semiconductor.

(3) Charge transfer from the semiconductor to the electrolyte.

(4) Generation of PEC voltage for water decomposition.

## 2.3 Photoelectrochemical Water Splitting

The basic principle of the process of photoelectrochemical water splitting (PEC) is the conversion of photons to electricity. It is an uphill reaction that needs a minimum Gibbs free energy ($\Delta G^{o}_{H2O}$) is 237.12 kJ/mol at standard temperature and pressure. In the simplest way to explain the process, through the external minimum energy water can be split to oxygen and hydrogen in a photoelectrochemical cell, as shown in **Figure 2.4**.

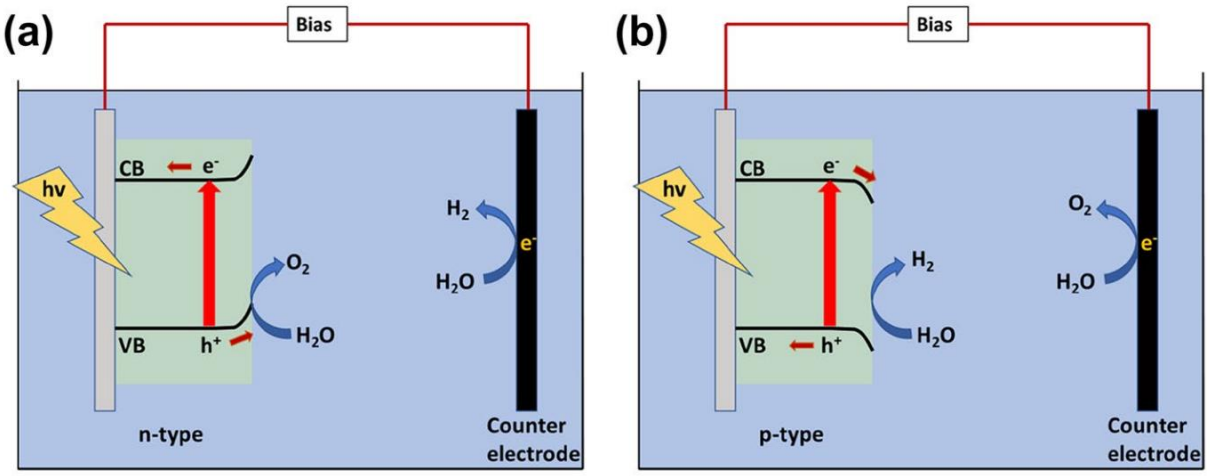


**Figure 2.4** Photoelectrochemical process for (a) n-type semiconductor, and (b) p-type semiconductor [20].

### 2.3.1 Reaction Mechanism

In this thesis, the focus will be on p-type semiconductors that are used as photocathodes, as copper oxides tend to act as photocathodes deriving water reduction reactions. In an aqueous electrolyte, the water splitting reaction using a p-type photocathode and a metal counter electrode (anode) involves several processes :

(1) The photocathode absorbs photons resulting in the formation of electrons-hole pairs:

$$h\upsilon + SC \rightarrow 4h^{+}+4\ e^{-} \qquad (2.5)$$

It is worth noting that this reaction only takes place if the incident photons have energy higher than the bandgap of the material. To avoid recombinations between the excitons, an electric field is required.

(2) The reduction process takes place at the photocathode:

$$4H^{+} + 4e^{-} \rightarrow 2H_2 \qquad \text{(HER, 0V vs RHE)} \qquad (2.6)$$

(3) The oxidation process of the water , which takes place at the anode through the

electrolyte, takes place at the metal counter electrode:

$$2H_2O + 4h^+ \rightarrow O_2 + 4H+ \qquad \text{(OER, 1.23 V vs RHE)} \tag{2.7}$$

(4) Accordingly: The overall reaction can be expressed as:

$$2H_2O \rightarrow O_2 + 2H_2 \tag{2.8}$$

The required energy to do this reaction is 1.23 eV. Accordingly, water decomposition is possible when the electromotive force of the cell is 1.23 V or more. Theoretically, photons that have an energy of 1.23 eV have wavelengths of about 1000 nm, which should be adequate for the PEC process. In practice, smaller wavelengths are required. This extra energy is to consider the losses due to recombination of the excitons, voltage losses at the contact, and electrode overpotential. The estimated value of these losses is about 0.6 V [21]. Therefore, the PEC cell needs at least 1.83 V to derive the PEC reactions.

## 2.4 Materials Requirements

To consider a material for PEC water splitting to act as a photocathode, several factors need to be considered such as the bandgap of the material, the straddling of the band offsets to the oxidation and reduction potential of water, high corrosion resistance and sustainability towards self-corrosion, and rapid charge transport kinetics. In addition, the materials should consist of earth-abundant elements and have low-cost fabrication techniques. The required properties for PEC water splitting have been identified, however, it is still a challenge to find a material that meets all requirements.

### 2.4.1 Bandgap

According to the bandgap criteria, p-type semiconductors such as CuO, $Cu_2O$, and $CuFeO_2$ should show visible light absorption. This criterion will determine the upper limit of the theoretical solar-to-hydrogen (STH) conversion efficiency. For instance, a p-type $Cu_2O$ with a bandgap of 2 eV has a theoretical STH of ~ 18%. However, bandgap is not the only criterion

to guarantee that PEC reactions will occur. The conduction band edge of the p-type semiconductor must be more negative than that of the hydrogen reduction potential. **Figure 2.5** shows the band alignment of several p-type metal oxide semiconductors [22].

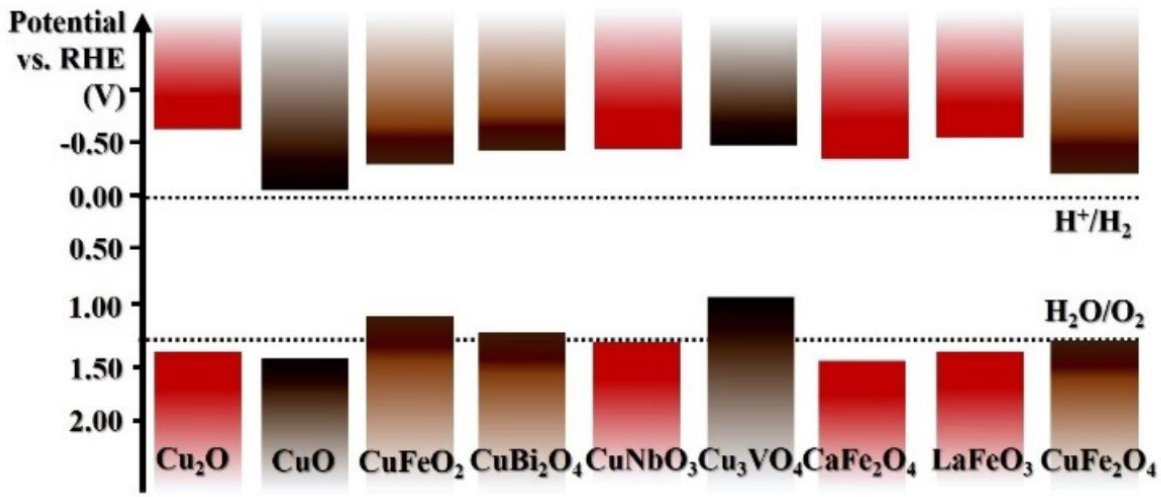


**Figure 2.5** Conduction Band and Valence Band edges for p-type semiconductors used in PEC [22].

### 2.4.2 Corrosion and Photocorrosion Resistance

It is necessary for the photoelectrodes to be stable in aqueous electrolytes before their usage in PEC. Otherwise, the PEC reactions will result in degradation of the properties of the photoelectrodes. An important question to be addressed in photoelectrochemistry is whether the occurring reaction is due to the reduction of water or due to the reduction of the p-type photoelectrodes themselves. Thus, Gerischer put the following rules for testing the stability of photoelectrodes against corrosion for the photoanode and the photocathode, respectively, as further illustrated by **Figure 2. 6**

$$\mathbf{E(O_2 \,/\, H_2O) < E_{p,d}} \quad (2.9)$$

$$\mathbf{E(H^+ \,/\, H_2) > E_{n,d}} \quad (2.10)$$

**where** $\mathbf{E_{p,d}}$ is the free enthalpy of oxidation per one electron-hole and $\mathbf{E_{n,d}}$ is the free enthalpy

of reduction per one electron.

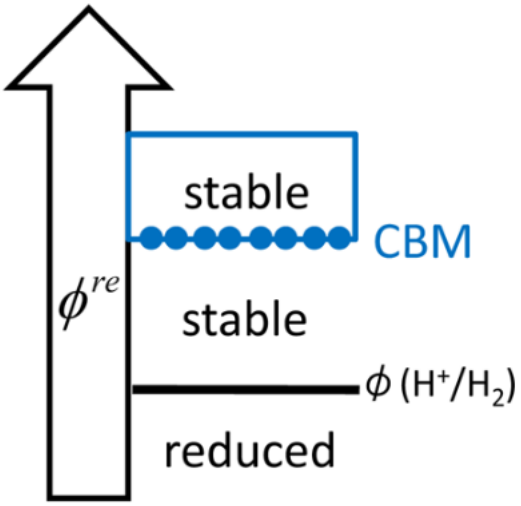


**Figure 2. 6** Relationship between reduction potential (Φre ) and the stability of the photocathode with respect to hydrogen reduction potential Φ [23] .

**Figure 2.7** shows the calculated thermodynamic oxidation and reduction potentials for several photoanodes and photocathodes used in PEC. The ab initio methods used to calculate the value of these potentials are beyond the scope of this thesis, but it could be a potential topic for very interesting research[23].

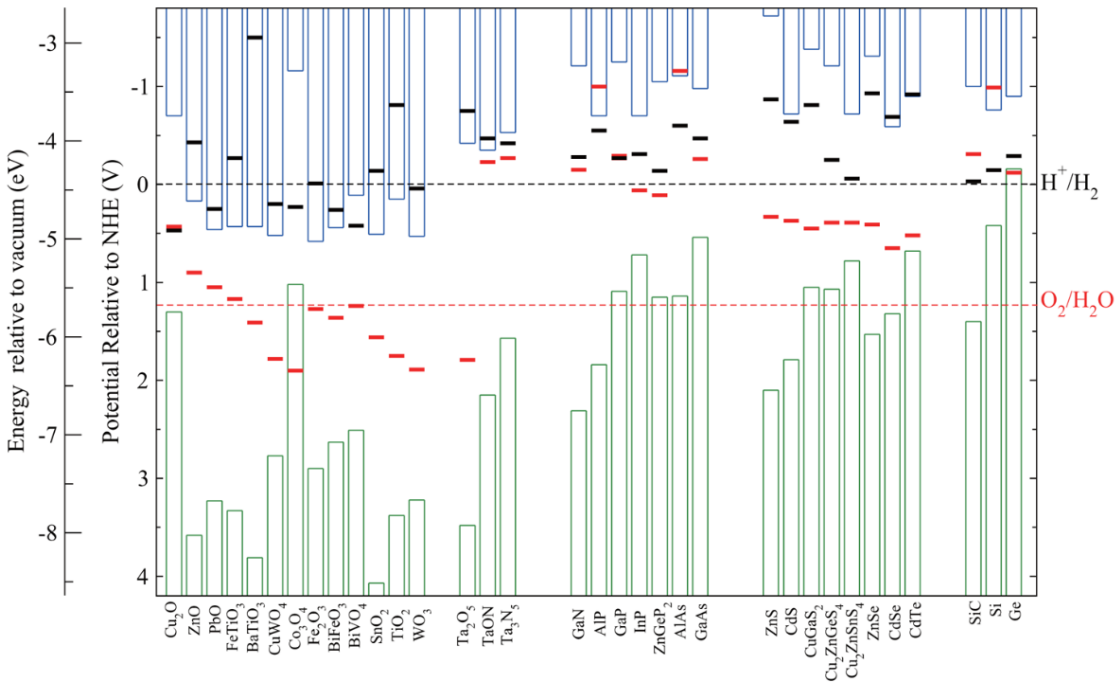


**Figure 2.7** Calculated thermodynamic oxidation and reduction potential of several materials that can be used in PEC [23]. (The red line is for thermodynamic oxidation potential, and the black line is for thermodynamic reduction potential).

Through the above figure, it can be concluded that p-type semiconductors such as $Cu_2O$ are unstable in an aqueous electrolyte during the PEC process and this instability is the main limiting factor beyond the further use of copper-based photocathodes. The redox potential of Cu+ is positioned below the redox potential of water, making it easier for the electrons to reduce Cu+ to Cu.

### 2.4.3 Avoiding Losses in Photoconversion Process

The rate of charge carrier recombination will determine whether the charge carriers will recombine or reach the semiconductor-electrolyte interface to derive the oxidation or reduction reactions. The radiative or non-radiative recombinations will lead to reducing the efficiency of

the PEC process. The presence of a direct bandgap of the material is preferable in terms of light absorption. However, the presence of an indirect bandgap is preferable in terms of slowing the recombination rate. An applied bias can impede the charge carriers recombinations, as proved experimentally. Therefore, the desired reactions can take place [24].

Fast charge carrier transport is also essential to avoid resistive losses during PEC water splitting. We need to explain the process more fundamentally to understand that part. For example, if a p-type semiconductor with a lower Fermi level of electrons than water is put in an aqueous solution, then the electrons will flow from the solution to the semiconductor, leading to the accumulation of electrons and depletion of holes at the semiconductor surface. The hole concentration at the semiconductor's surface is lower than the hole concentration at the semiconductor's bulk. Therefore, an electric field will develop inside the semiconductor pointing from the semiconductor-electrolyte interface toward the bulk of the semiconductor. As a result, electrons at the interface have a lower energy than electrons in the bulk of the semiconductor, which will result in a downward band bending. When the semiconductor is illuminated, the electrons will move from the VB to the CB leaving behind holes bringing the Fermi energy closer to the CB. Due to the developed electric field, holes are pushed away to the bulk of the semiconductor and electrons will be pushed toward the semiconductor-electrolyte interface being available to reduce water. This whole process is called "charge separation"[24]. For efficient charge transport, high conductivity is needed, which is governed by carrier mobility and carrier concentration. Carrier mobility is affected by impurities and defect concentrations; electrons and holes scatter due to crystallographic defects. Carrier concentration is determined by the doping level, temperature, and the intensity of illumination. These parameters can be reflected in a high resistance to charge transport.

# Chapter 3

# Literature Review

## 3.1 Nanostructured Photocathode Materials

Nanotechnology has contributed to the development of efficient and innovative approaches for the fabrication of organized structures that can be utilized for various applications. These structures include zero-dimensional nanomaterials such as nanoparticles, one-dimensional nanomaterials such as nanowires, nanotubes, and nanorods, and two-dimensional nanomaterials such as nanocomposites. Nanomaterials are unique structures due to their large surface area, superior mechanical properties, and controlled charge transfer pathway. The challenge that scientists and engineers face is how to optimize the fabrication of nanomaterials.

Of these materials, photocatalytically active metal oxides are of high importance in the field of PEC water splitting to produce hydrogen. The most challenging metal oxides to deal with in the field of PEC water splitting are p-type semiconductors due to their instability in aqueous electrolytes, as explained in Chapter 2. The types of metal oxide photocathodes include binary metal oxide photocathodes and ternary metal oxide photocathodes. For the scope of this thesis, we will focus on copper-based photocathodes.

## 3.2 Binary Cu-based Oxides Photocathodes

Copper oxides ( CuO and $Cu_2O$) have attracted so much attention in the realm of PEC water splitting owing to their unique chemical and physical properties. They have narrow bandgaps, and they are earth-abundant and non-toxic elements. However, the chemical instability of these materials has been an issue in their large-scale application and it has been

addressed by surface passivation by the usage of protective layers, interfacial engineering, and co-catalyst modification.

### 3.2.1 $Cu_2O$

Cuprous oxide is a naturally occurring p-type semiconductor. The p-type property originates from the Cu vacancies. The valence band of the p-type $Cu_2O$ is formed by the hybridization of Cu 3d and O 2p bands. It crystallizes in a simple cubic structure. The unit cell contains four copper atoms and two oxygen atoms. The minority carrier diffusion length of $Cu_2O$ is in the range of 1-10 μm when a high Hall mobility is assumed. The direct bandgap of 2 eV leads to a theoretical efficiency of 18.1%, which makes $Cu_2O$ a promising candidate for PEC water splitting. In addition, the conduction band edge is appropriate for water reduction reaction, while the valence band edge position makes it unfavorable for oxygen evolution reaction (OER). The only drawback of $Cu_2O$ is that the reduction potentials of copper lie within the band gap making it more favorable to reduce $Cu_2O$ into metallic copper instead of reducing water. Therefore, coating the $Cu_2O$ light-absorbing layer with an n-type semiconductor facilitates the diffusion of minority charge carriers to the semiconductor-electrolyte interface. Furthermore, the n-type semiconductor protective layer needs to have a conduction band that is more negative than $Cu_2O$, as the photovoltage is defined as the difference between the Fermi levels of the $Cu_2O$ and the n-type semiconductor. In addition, a co-catalyst is usually needed to promote the catalytic reaction on the photocathode and improve its stability. Even though there were many attempts to stabilize $Cu_2O$ and to obtain high photovoltage. It remains a challenge to achieve a high STH conversion efficiency for the usage of $Cu_2O$ photoabsorbers in commercial applications. This inefficiency is due to the bulk charge recombination and bulk defects. Dopinf can be introduced to tune the carrier density, mobility, and conductivity[25].

### 3.2.2 CuO

Cupric oxide is an intrinsic p-type semiconductor with a narrow bandgap of 1.2-1.5 eV. Thus, CuO is a good photoabsorber to harvest a significant portion of the solar spectrum. CuO has a monoclinic crystal structure. The conduction band edge of CuO is more negative than the water reduction potential. Therefore, CuO is suitable for water reduction reactions. Even though this material is promising, little research has been focused on it due to the limitations associated with it. CuO is prone to photocorrosion as the reduction potential of CuO lies within the bandgap. At first, it is degraded to $Cu_2O$, then it is reduced to metallic Cu. Moreover, CuO has low charge separation efficiency meaning that photoexcited electrons and holes might recombine before reaching the semiconductor-electrolyte interface. Even though several reports tried to stabilize CuO by nanostructuring, and plasmonic metals, these approaches were not successful, as self-reduction was inevitable as evident by the presence of a large dark current. Thus, the usage of protective strategies is also important to avoid photocorrosion and enhance charge carrier separation. Measuring the amount of hydrogen and the Faradaic efficiency is also important to make sure that the photocurrent is due to hydrogen production, not copper reduction [25].

### 3.3 Strategies to Stabilize Cu-based Photocathodes

The main struggle that hinders the development of PEC water splitting is finding a photocathode that withstands the conditions of PEC in an aqueous electrolyte. Photocathodes are unstable in long operation conditions. As cupric oxide is a promising photocathode due to its low bandgap, low cost, and nontoxicity, several efforts have been made to stabilize cupric oxide. Li et al stabilized cupric oxide through the usage of an alkaline environment and low-intensity light. This was proved by the retention of 100% of the photocurrent after 20 minutes of illumination. It is worth mentioning that this stabilization strategy was accompanied by the deposition of a protective layer of $TiO_2$, $La_2O_3$, and NiO. The stabilized photocurrent is

measured as 0.3 mA/cm$^{-2}$ at 0.5 V vs RHE [26]. Cots et al stabilized CuO nanowires by the adsorption and drop-casting of Al. Thermal treatment is applied after Al modification. The Al modification blocked the self-reduction active sites making the water reduction the more favorable reaction [27]. Furthermore, Cots et al tried to stabilize cupric oxide without the usage of a co-catalyst by the impregnation method of a solution containing iron followed by a thermal treatment to form a ternary copper iron metal oxide. After incorporating iron in the structure, the Faradaic efficiency (FE) reached ~100% which is better than the FE of the unprotected cupric oxide nanowires that only reached 45% over the course of 45 mins [28]. It is worth mentioning that even though the stability was improved, this improvement was at the cost of photocurrent. Oh et al stabilized cupric oxide through the usage of nickel-doped cupric oxide seed layers with various doping concentrations. It was found that Ni atoms that diffused into the structure reduced the dark current, as they prevented the reduction of the metal oxide. However, the highest photostability obtained was 46.2% using 10 at% of Ni doping. The stability was measured by the retention of the photocurrent [29].

Stabilization of cupric oxide can also be through the deposition of co-catalysts such as Pt. The co-catalysts on the surface of the CuO photoelectrodes accelerate surface reactions preventing charge accumulation at the semiconductor-electrolyte interface, which results in a significant improvement in the stability of the photocathodes [30].

Another method to stabilize cupric oxide is through the formation of a p-n junction. Shaislamov et al stabilized cupric oxide by growing CuO nanorods on a Cu foil, then growing ZnO nanobranches uniformly by hydrothermal method. The stability was enhanced by 90% due to the formation of a dense layer of ZnO that prevented direct contact between CuO and the electrolyte. However, this improvement in stability was at the cost of the PEC performance. This can be attributed to the increased charge transfer resistance and the hindrance of the optical

absorbance of CuO [31]. The protective overlayers that are in direct contact with the electrolyte have a large overpotential for the HER. Thus, co-catalysts should be added to facilitate the reaction. Xing et al stabilized CuO by the usage of a $TiO_2$ protective layer and Pt as a co-catalyst. The CuO/ $TiO_2$/Pt electrode showed PEC performance improvement compared to pristine CuO electrodes and CuO/$TiO_2$ electrodes. This previous work proves that the combination of a heterojunction and a cocatalyst improves the PEC performance [32]. However, this technique suffers from the Pt either dislodging from the surface or being poisoned by the impurities in the electrolyte [33].

Another method to stabilize CuO is through the usage of protective layers. Kunturu et al tried to stabilize CuO through the usage of a protective layer consisting of a thin carbon layer. In this study, the optimized electrodes showed photocurrents up to 6.5 mA/$cm^{-2}$ at 0V vs RHE. The photocurrent was retained after 50h of continuous illumination at 0.3 V vs RHE, with the absence of a cocatalyst, compared to the electrodes without the thin carbon layer. The enhancement of the stability is due to the effective charge transfer and the usage of a protective layer that prevents direct contact between CuO and the electrolyte [34]. In some studies, the protective layers can be coupled with metals to enhance light absorption. Xing et al fabricated a CuO/Al/$Al_2O_3$ photoelectrode, where CuO was the photoabsorber, Al was a light absorption enhancer through surface plasmon resonance, and $Al_2O_3$ acts as a protective layer. The photocorrosion stability was measured through the retention of 90% of the photocurrent after 1 hour of continuous illumination, which is a 50% improvement compared to the bare CuO.

### 3.4 Fabrication of Brass-based Electrodes by Anodization

Copper-zinc-based bimetallic chemistry has gained lots of attention owing to their catalytic applications, and mechanical properties. Brass alloys exhibit superior electrical and thermal conductivity, corrosion resistance, and enhanced mechanical properties compared to pure copper. Several attempts were made to produce nanostructured brass-based electrodes for

several applications.

During the last few decades, simple anodic oxidation of metals (Anodization) has become a very promising approach to synthesize semiconducting metal oxides. Anodization is a technique to produce metal oxide thin films on a metal substrate. One of the extensively studied metals is titanium. **Figure 3. 1** shows a schematic diagram of the anodization process to Ti foil. In this process, a protective layer is formed over the metallic substrate. The thickness and the density of the oxide layer depend on the control over the oxidation parameters. Overall, the anodization cell consists of two electrodes (anode and a cathode) connected to a power supply. In our study, brass is the anode, and graphite rod is the cathode. The cathode needs to be of a material that is resistant to the reaction process such as Pt or graphite. The last component of the anodization cell is the electrolyte. It mainly consists of water and an ion that handles the itching process. The choice of electrolyte plays a decisive role in determining the morphology of the structure. Anodization potential, temperature, and time are also factors in determining the morphology of the structure [35]. It is proven that nanostructured CuO and ZnO can be obtained by anodic oxidation of copper and Zn in basic electrolytes. Both have important applications in energy conversion and storage fields. The combination of both semiconductors and the formation of a p-n junction helps with the charge separation of the photoexcited charge carriers making it more efficient. Thus, the direct anodization of brass is of great interest. Dezfoolian et al have investigated the anodization of brass in alkaline electrolyte (KOH). This process resulted in the formation of nanostructured products consisting of CuO phase and ZnO phase. The morphology of the resulting nanostructures heavily depends on the applied conditions. Eissa et al investigated the anodization of brass in sodium bicarbonate solution, then the anodization was followed by annealing of the nanostructures. This treatment resulted in the formation of CuZnO nanoparticles or nanowires depending on the electrolyte concentration. Then, the

resulting samples were tested for PEC water splitting. Ryczek et al presented a fast anodic formation of nanoparticulate CuO and ZnO by anodization in a strongly alkaline electrolyte. The obtained layers consisted mainly of the CuO phase with a higher content of ZnO within the deeper parts of the anodized films [36–38].

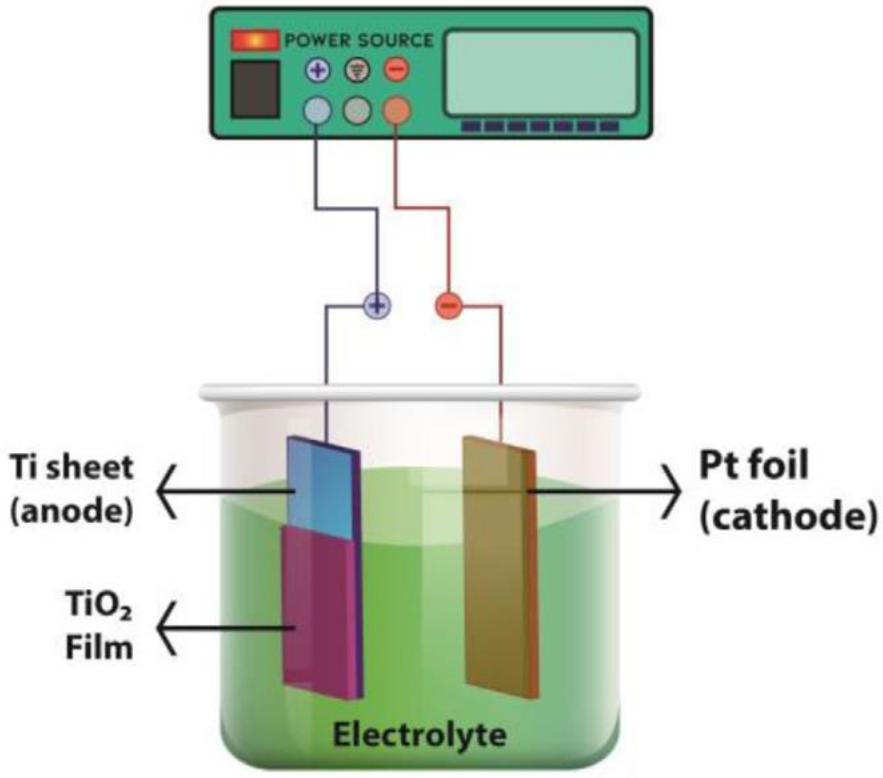


**Figure 3. 1** Figure 3.1 Anodization process to Ti foil using Pt as a cathode and Ti as an anode [35].

# Chapter 4

# Experimental Methods and Materials

## 4.1 Potentiostatic Anodization and Thermal Annealing

In this work, four commercial brass alloys and a Cu foil were used to test their PEC performance. The commercial brass alloys contained different concentrations of Zn. The first sample contained 95% Cu and 5% Zn. The second sample contained 85%Cu, and 15% Zn, and the third sample contained 70%Cu, and 30%Zn. The fourth sample contained 50%Cu, and 50% Zn, while the fifth sample was pure copper. The samples were tagged 95Cu-5Zn, 85Cu-15Zn,70Cu-30Zn, 50Cu-50Zn and 100Cu.

Before Anodization, the samples were mechanically polished using coarse, medium, and fine SiC grinding paper. Then, the samples were polished with an alumina-wetted cloth to remove any residuals from the polishing step. Then, the samples were ultrasonically cleaned in acetone, followed by ethanol, and followed by deionized (D.I.) water; each for 10 mins. The anodization process was performed according to the method described by Bahnsawy et al in a two-electrode electrochemical cell connected to DC Agilent (E3612A) power supply with the brass or Cu foil as the working electrode, and graphite rod working as counter electrode under a constant applied voltage of 4V at room temperature (approximately 25º C). The electrolyte consisted of 48 ml of DI water, 1 ml of 2.5 M NaOH, and 1 ml of 0.1M APS. The anodization time continued for five minutes [39]. The distance between the two electrodes was fixed at 1.5 cm. A schematic diagram of the anodization process is shown in **Figure 4.1**.After the anodization process, the samples were rinsed thoroughly with deionized water, then they were blow-dried with air.

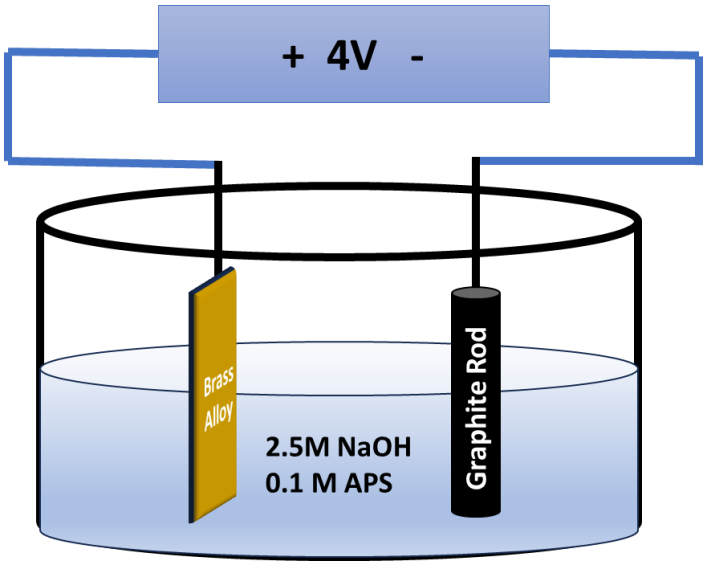


**Figure 4.1** Schematic Diagram of the anodization process to the Cu foil and Brass Alloy

After the anodization process, the resulting films were put in a quartz tube inside a Thermo scientific tube furnace to be annealed in air at 350 ºC. All the samples were subjected to thermal air annealing under a constant 50 SCCM flow rate with a heating and cooling rate of 5 ºC /min.

## 4.2 Materials Characterization

- The morphological structure of the as-anodized and as-annealed samples was explored using Field Emission Scanning Electron Microscope (Zeiss SEM Ultra 60 FESEM machine).
- Energy Dispersive X-ray (EDX; Oxford ISIS 310, England) spectroscopy was used for the elemental analysis and mapping of the fabricated electrodes.

- The crystal structure of the annealed samples was determined using PANalytical X-pert Pro PW3040 MPD X-ray diffractometer through monochromatic radiation (Cu-Kα, λ=0.15406 nm, 50 mA,40 kV) in the range of 5°–80° with a glancing angle of 2°.
- Renishaw InVia dispersive Raman spectrometer equipped with a Leica DM microscope and a Renishaw HeNe 532 nm laser was used to characterize the vibrational modes as well as the phase composition of the annealed samples.
- X-ray Photoelectron Spectroscopy (XPS) was used to deeply understand the surface composition of the as-anodized and as-annealed samples. Thermo Scientific Kα X-ray Photoelectron Spectrometer was used and the measurements were done in UHV champer with Al Kα monochromator. The C1s binding energy (284.4 eV) of adventitious carbon was taken as the reference. CasaXPS software was crucial for the deconvolution of the peaks and fitting of the obtained data. In addition, the valence band maximum edge was determined with the aid of XPS by the analysis of the spectrum at very low binding energies.
- The optical properties of the samples were studied using a Shimadzu UV-Vis diffuse reflectance spectrometer in the range of 200-800 nm, and the bandgap of the sample was calculated accordingly using Tauc plot.
- Thermoscientific ESCALAB250 Xi Ultraviolet Photoelectron Spectroscopy (UPS) was used to determine the band offsets of the annealed samples.

### 4.3 Photoelectrochemical Analyses of the samples

Photoelectrochemical measurements were conducted in 0.1 M sodium carbonate (pH=11.7) in a three-electrode cell configuration with Hg/HgO as a reference electrode, Pt as a counter electrode, and the annealed samples as the working electrode. The measurements were done using a Bio-Logic SP 200 potentiostat equipped with a solar simulator (300 W

Ozone-free Xenon lamp under 100 mW/cm$^2$ illumination and with AM 1.5G filter). The scan rate was 10 mV/s. Open circuit voltage (OCV) measurements, Linear Sweep Voltammetry (LSV) measurements, cyclic voltammetry, Chronoamperometry measurements, Electrochemical Impedance Spectroscopy (EIS) measurements, and Mott Schottky (M-S) measurements were conducted.

### 4.3.1 Open Circuit Voltage (OCV) measurements

OCV is used to determine the photovoltage and to determine the conductivity type of the sample. If OCV moves in the positive direction under illumination, then the sample is a p-type semiconductor. If the OCV moves negative, then the sample is an n-type semiconductor. If the material is not affected by the OCV test, then it is unlikely to show a photo response to any other PEC performance test. This is because OCV is a measurement of the Fermi level splitting (quasi fermi level) in a semiconductor [40]. In this work, the OCV measurements were done under chopped illumination, which helped with determining the type of the semiconductor and calculating the decay lifetime of the tested samples [41].

### 4.3.2 Cyclic Voltammetry (CV) measurements

CV is a fundamental electrochemical technique that provides information about electrochemical behavior of semiconductors in a current vs potential graph. To further investigate the photocathodes, cyclic voltammetry was performed both under illumination and under dark conditions. Through CV measurements, it is possible to detect the photo response of the photocathode[42].

### 4.3.3 Linear Sweep Voltammetry (LSV) measurements

LSV is used to measure the dark and photocurrent of the samples as a function of the applied potential; to have an idea about the photocurrent of the sample, we use the

relationship that photocurrent = current under light illumination – dark current. Through LSV, one can determine the onset potential of the samples, and the photocurrent density.

### 4.3.4 Chronoamperometry (CA) measurements

CA measurements make it possible to test the stability of the photocathodes through long-term illumination over a long period of time, or chopped illumination over a short period of time. The chopped illumination enables the calculations of transient time constant [41]. Chronoamperometry under chopped and continuous illumination was performed to determine the stability of the sample at 0.62 V vs RHE

### 4.3.5 Electrochemical Impedance Spectroscopy (EIS) measurements

EIS is based on the perturbation of an electrochemical system that is in equilibrium through the application of a sinusoidal signal over a wide range of frequencies. Then, the sinusoidal response of the system towards the applied perturbation is monitored. In this study, EIS measurements under dark and light conditions with a frequency range from 1MHz to 50 mHZ enabled the study of surface states and the interfaces that exist in the system.

### 4.3.6 Mott Schottky (M-S) measurements

Mott Schottky Analysis is a technique used to perform successive impedance measurements on a whole frequency range during a potential scan or a current scan. Then, the Mott-Schottky plot ($1/C^2$ vs E ) is displayed and a linear fit can be used to extract the parameters of the semiconductors such as flatband potential and charge carrier density. In this study, M-S measurements are done under dark conditions to calculate the flatband potential and the concentration of the charge carriers' density.

## 4.4 Hydrogen Quantification

To quantify the amount of hydrogen produced using the 100 Cu and 95Cu-5Zn samples, a 3-electrode cell was designed. Nitrogen gas was made to flow through the cell at a controlled rate. The outlet of the cell was directed towards the inlet of a gas chromatograph (GC), where the gas is analyzed at the set times of 20, 40, and 60 min. The applied voltage was 0.62 V vs RHE throughout the measurements.

### 4.5 Computational Methods

Computational calculations were conducted for the 95Cu-5Zn sample. All calculations were based on a spin-polarized density functional theory and were performed using the standard Cambridge Serial Total Energy Package (CASTEP), as implemented in Materials Studio 2017. Generalized gradient approximation (GGA) and the Perdew-Burke-Ernzerhof (PBE) exchange-correlation functional were used for geometry optimization, electronic property calculation, and adsorption energy computation. The interaction between electrons and ions was represented using an OTFG ultrasoft pseudopotential, where the Broyden-Fletcher-Goldfarb-Shanno (BFGS) algorithm was utilized with a cutoff energy of 630 eV and a separation distance of 0.07 Aº for the K-points. Convergence was ensured by relaxing the bulk structure of CuZnO, until it met the convergence criteria of less than $5.0 \times 10^{-6}$ eV/atom, 0.01 eV/ Aº, 0.02 GPa, and $5.0 \times 10^{-4}$ Aº for the energy, force, stress, and displacement, respectively.[43] The optimized lattice constants for the bulk CuZnO were determined to be a=7.21 Aº, b=5.38 Aº, c=9.63 Aº, $\alpha = \gamma = 90^{o}$, and $\beta = 89.81^{o}$, providing valuable insights into the structure of the material. To obtain a more accurate electronic band structure diagram, DFT+U calculations were performed to avoid the self-interaction error that often leads to a significant underestimation of the band gap. A Hubbard correction value of 9 eV was set for Cu's d orbitals. Given that the hydrogen evolution reaction is most favorable on the (-1 1 1) facet, which is the dominant facet in our material, a cleaved surface of (-1 1 1) was

utilized to build a bulk crystal with a vacuum slab of 15 Aº in the Z direction. This approach prevented interaction between the periodic layers and allowed for an accurate analysis of the material's electronic properties.

# Chapter 5

# Results and Discussion

# (Materials Characterization)

As mentioned in the previous chapters, the main hindrance to PEC development is finding a stable photocathode that withstands the PEC conditions. This will enable the production of green hydrogen allowing the closure of the carbon cycle and eliminating $CO_2$ emission providing essential tools to combat climate change. According to Chapter 3 discussion, Cu-based photocathodes are promising for PEC, yet they are difficult to deal with in terms of stabilization in aqueous electrolytes to split water. However, their advantages such as low cost, earth abundance, and low bandgap make scientists and researchers interested in pursuing further research for stabilization. Despite many efforts, as discussed in Chapter 3, it remains a question whether cupric oxide will make it to the market and be large-scale in the field of PEC by proper stabilization. In this chapter, we try to address our findings when employing anodized and then annealed brass-based alloys and copper foil in PEC. Given the primary goal of this work is to stabilize cupric oxide, brass alloys were used as it contains Zinc that can work as a copper stabilizer. ZnO is an n-type semiconductor that is very stable in aqueous electrolytes. Accordingly, a set of parameters has been determined to enhance the PEC performance of cupric oxide using alloying with Zn, as will be discussed below. In this regard, it is expected that Zn alloying is going to stabilize cupric oxide making it less prone to photocorrosion. To this end, this chapter includes the results of the characterization techniques used to analyze the as-anodized and as-annealed brass alloys and Cu foil. This chapter is divided into three main

sections. The first section discusses the SEM imaging and EDX elemental mapping of the as-anodized and as-annealed samples. The second section discusses the phase analysis of the as-anodized and as-annealed samples by XRD and Raman Spectroscopy, and the third section deeply discusses the surface analysis of the samples using XPS and UPS.

## 5.1 Morphological Analysis of the Synthsized Nanostructures

95Cu-5Zn, 85Cu-15Zn,70Cu-30Zn,50 Cu-50Zn and 100 Cu samples were synthesized via the anodization of commercial scrap brass alloys and Cu foil. Prior extensive experiments showed that the anodization of copper-based alloys showed polyhedral, nanorods, nanowires, and nanoparticle structures based on the anodization conditions. **Figure 5.1** depicts the morphology of the as-anodized nanostructures. The morphology of the films shows uniformly distributed nanoparticle structures of the samples before anodization. **Figure 5. 2** shows the SEM images of the structures after annealing. The figure shows a uniform distribution of the nanostructures over the samples (brass substrates). It can be noted in Figure 5.3 that the increase in Zn content leads to agglomeration as the particles tend to lower their surface energy. It is also worth mentioning that annealing the samples leads to fusion of grain boundaries leading to larger particle size. The change in morphology between Cu samples and other brass alloy samples might be attributed to the substitutional defects of zinc in the CuO lattice.

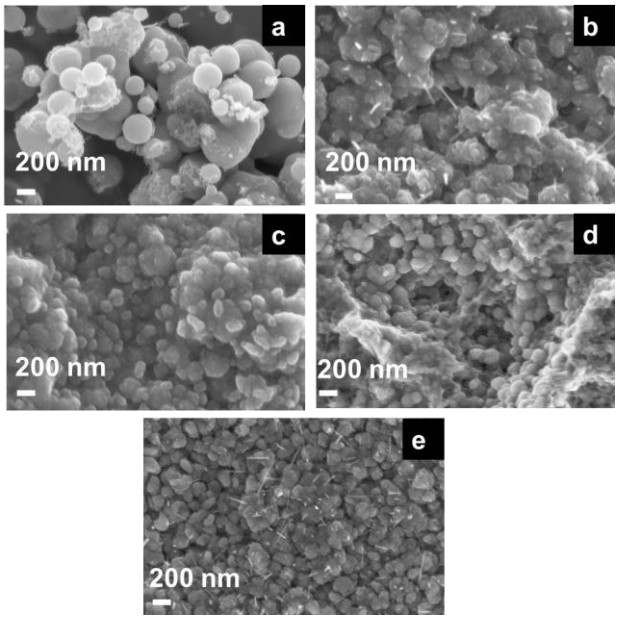


**Figure 5.1** SEM images for as-anodized (a) 95Cu-5Zn, (b) 85Cu-15Zn, (c) 70Cu-30Zn, (d) 50Cu-50Zn, and (e) 100 Cu.

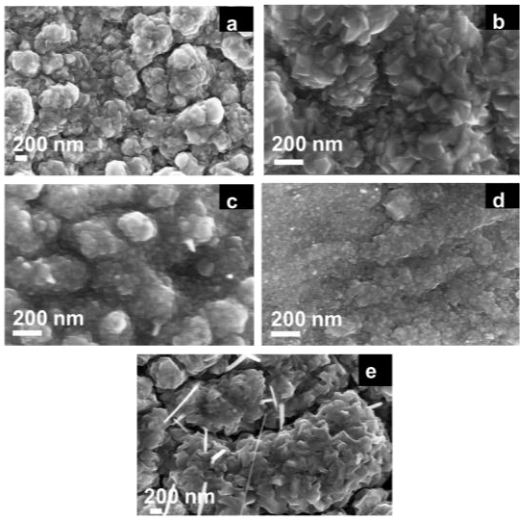


**Figure 5. 2** SEM images for anodized then annealed (a) 95Cu-5Zn, (b) 85Cu-15Zn, (c) 70Cu-30Zn, (d) 50Cu-50Zn, and (e) 100 Cu.

## 5.2 Compositional and Structural Analysis

In this study, we report for the first time the compositional and structural analysis of

anodized and annealed brass alloys, so that they will be an attractive and robust material for visible-light-driven photoelectrochemical water splitting. The details of the compositional and structural analysis using EDX, XRD, Raman spectroscopy, and XPS will be discussed below.

### 5.2.1 EDX Results

As mentioned in section 5.1, the SEM images of the anodized and the anodized then annealed samples revealed the homogenous distribution of the nanoparticle structure over the brass samples. To further unveil the effect of anodization and annealing on the samples, EDX elemental mapping is a necessary tool to reveal the elemental mapping of the samples. **Figure 5.3** shows the elemental composition of the five anodized samples. It can be noted that the elements (Cu, Zn, O) are uniformly distributed over the surface of the sample.

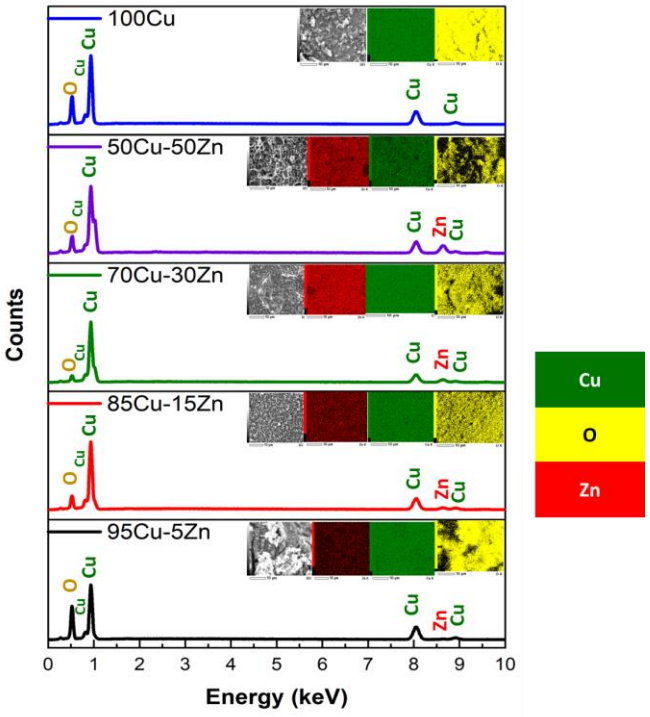


**Figure 5.3** EDX analysis for the samples after being anodized.

Further elemental analysis for the annealed samples after annealing is shown in **Figure 5.4**. Through this figure, we can notice the uniform distribution of elements in the samples.

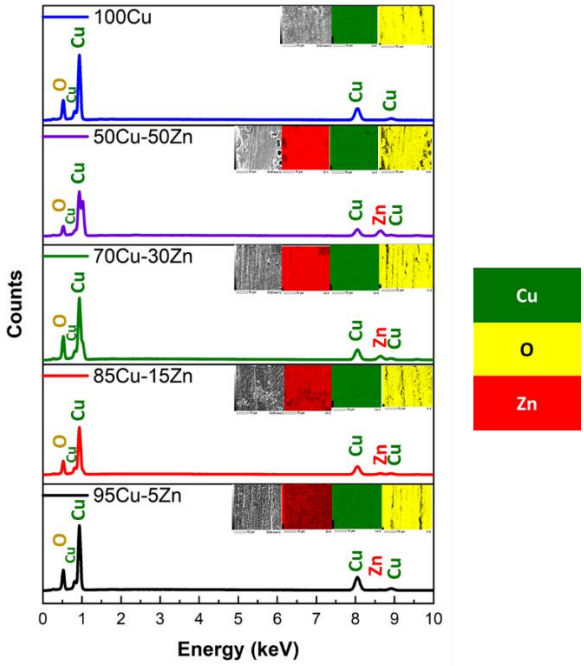


**Figure 5.4** EDX analysis for the samples after being annealed following anodization.

### 5.2.2 XRD Results

**Figure 5.5** shows the XRD results of the annealed samples. There are sharp XRD peaks, which implies that the samples are crystalline. The three main peaks in the samples are characteristics of the α-brass alloy (substrate) representing rhombohedral Cu-Zn at 42.83º (110), 43.82º (104), and 49.65º (112) (ICDD: 00-025-0322). The XRD pattern of samples 95Cu-5Zn shows peaks at 35.93º, 38.68º, 51.03º, and 61.86º attributed to the (-111) monoclinic CuO, (111) monoclinic CuO (ICDD: 01-080-0076), (200) cubic copper (ICDD: 00-003-1005), and (-113) monoclinic CuO (ICDD: 01-080-0076), respectively. Sample 85Cu-15Zn shows similar peaks to sample 95Cu-5Zn attributed to monoclinic CuO, rhombohedral Cu-Zn, and cubic copper. Sample 70Cu-30 Zn did not show peaks for monoclinic CuO, even though it showed a p-type semiconductor behavior, according to Mott-Schottky calculations that will be presented later. This might be because the metal oxide thin film on the brass substrate is too thin to be detected by XRD. The sample 50 Cu-

50 Zn only showed two main peaks of rhombohedral Cu-Zn showing no peaks for the oxides, which can also be attributed to the limitations of XRD measurements. Sample 100Cu showed peaks at 29.32º, 36.23º, 38.28º, 41.92º, 42.73º, and 60.76º attributed to (110) cubic Cu2O (ICDD: 01-078-2076), (111) cubic Cu2O, (111) monoclinic CuO, (200) cubic Cu2O, (111) cubic copper, and (-113) monoclinic CuO, respectively. It is worth noting that in samples (95Cu-5Zn, 85Cu-15Zn), a single phase of monoclinic CuO was formed implying that there is no phase segregation up to 30% alloying of copper when the samples are anodized and annealed, which means that zinc ions substituted copper ions in the lattice. This agrees well with the phase diagram of Cu-Zn alloy, which shows that Cu-Zn alloys exhibit a single α-phase below 35 wt.% Zn, above which the intermetallic β-phase would be formed [44]. Two phases of copper oxide were formed upon anodization and annealing of the 100Cu sample. It is also noted that as the concentration of Zn increases, the intensity of copper oxide peaks decreases, even though there were no distinct peaks for ZnO.

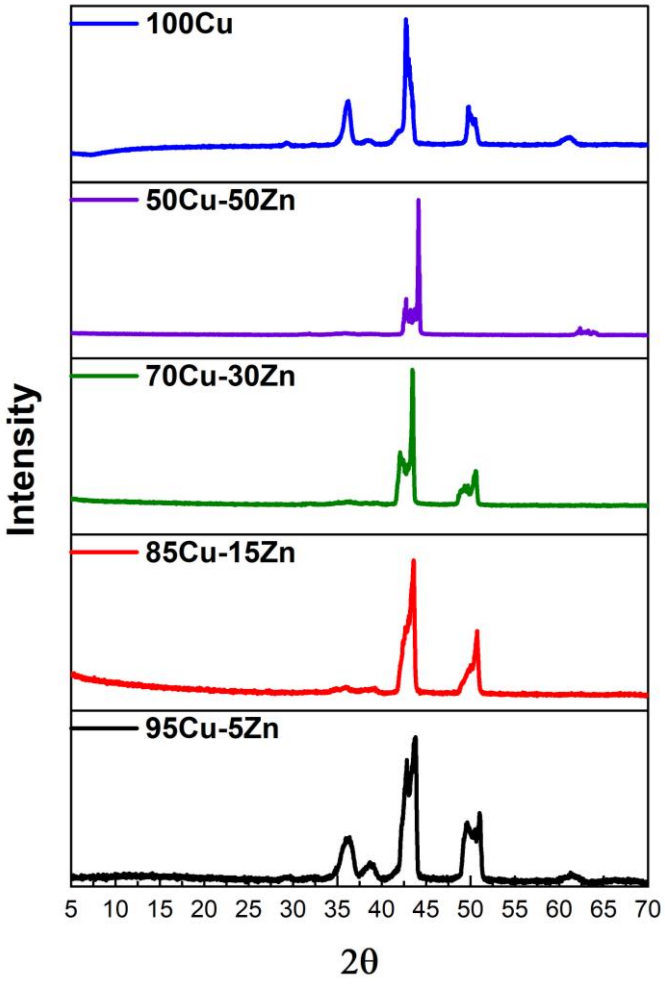


**Figure 5.5** XRD measurements for the samples.

The average crystallite size and strain introduced in the samples can be calculated using Williamson-Hall (W-H) plots according to Eq. 5.1

$$\beta \frac{\cos\theta}{\lambda} = \frac{0{\cdot}9}{d} + 4\varepsilon \frac{\sin\theta}{\lambda} \qquad (5.1)$$

where β is the half-width at half maximum, ε is the lattice strain, θ is the Bragg angle, d is the average crystallite size, and λ is the wavelength of the x-ray. To get the average crystallite size and lattice strain $\boldsymbol{\beta \frac{\cos\theta}{\lambda}}$ is plotted against $\boldsymbol{\frac{\sin\theta}{\lambda}}$ and fitted into a straight line, then the lattice strain can be obtained from the slope, and the average crystallite size from the intercept. The

relationship between the Zn content versus microstrain and crystallite size is shown in **Figure 5.6**. As the Zn content increases, average crystallite size decreases and lattice strain increases; implying that increasing Zn content increases the lattice imperfections, which will adversely affect the photoelectrochemical performance of the samples as will be illustrated later in Chapter 6.

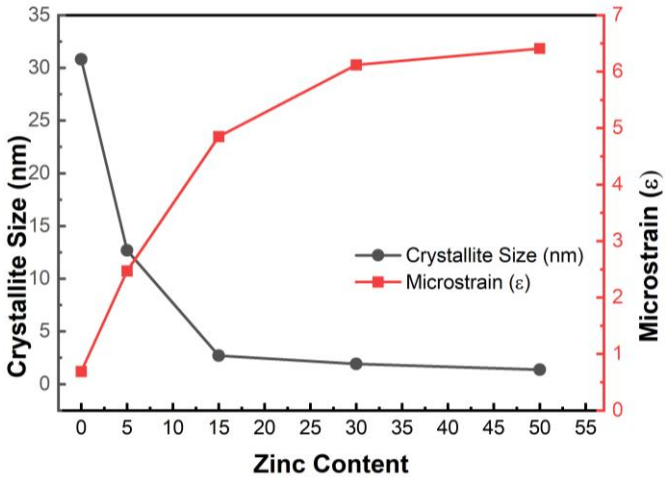


**Figure 5.6** Relationship between Zn content, crystallite size, and microstrain of the five studied samples.

### 5.2.3 Raman Spectroscopy Results

To further confirm the structural findings, Raman spectroscopy gives useful insights into whether secondary phases are formed for alloyed materials or not due to the introduction of foreign atoms in the host material. **Figure 5.7** shows the Raman spectra of the 95Cu-5Zn, 85Cu-15Zn, 70Cu-30Zn, 50Cu-50Zn, and 100Cu samples. Copper oxide forms two different oxides; cupric oxide and cuprous oxide. Cupric oxide has twelve phonon modes. The zone center optical phonon modes for CuO are $\boldsymbol{\Gamma = A_g + 2B_g + 4A_u + 5B_u}$.Three of these phonon modes are Raman active ($\boldsymbol{A_g, 2B_g}$) and the rest are infrared active. [45] The symmetry of

vibrational modes for $Cu_2O$ is $\boldsymbol{\Gamma = A_{2u} + E_u + 3T_{1u} + T_{2u} + T_{2g}}$. The only Raman active mode is $\boldsymbol{T_{2g}}$ symmetry [46,47]. The remaining modes are either infrared active or silent modes. For sample 100Cu, the peaks at 217.13, 297.52, 345.01, and 630 $cm^{-1}$ are attributed to $Cu_2O(\boldsymbol{E_u})$ silent mode, CuO $(\boldsymbol{A_g})$, CuO $(\boldsymbol{B_g})$,, and CuO $(\boldsymbol{B_g})$, which agrees with the XRD data. Sample 95Cu-5Zn shows the three Raman active phonon modes of CuO at 297.52, 345, and 630 $cm^{-1}$. Sample 85Cu-15Zn shows the three Raman active phonon modes of CuO at 299.42, 348.79, and 633.66 $cm^{-1}$. In addition, the $\boldsymbol{T_{2g}}$ Raman active mode of $Cu_2O$ appears at 569.34 $cm^{-1}$, proving that sample 85Cu-15Zn has a mixture of $Cu_2O$ and CuO, which was not obvious in XRD data. Sample 70Cu-30Zn shows Raman active modes of CuO at 297.52, 345, and 630 $cm^{-1}$ [48]. Sample 50Cu-50Zn shows no observable peaks in Raman spectra for cupric oxide or cuprous oxide, even though it shows p-type behavior.

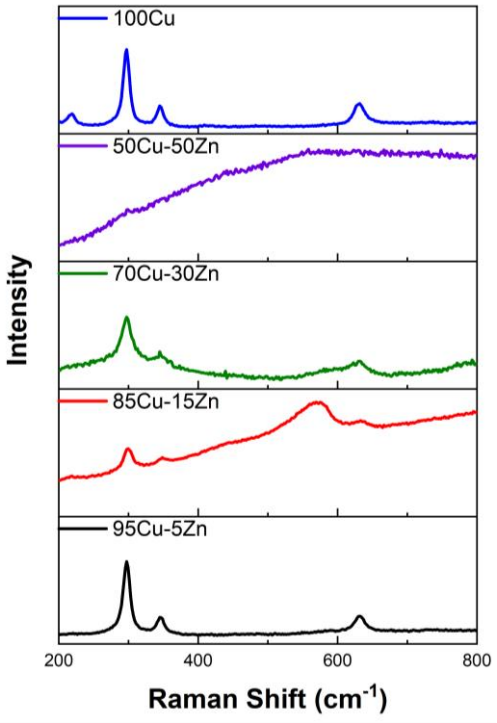


**Figure 5.7** Raman spectra for the five samples.

Raman spectra were also used to calculate the phonon lifetime of the samples as shown in **Table *0.1***[49]. The phonon lifetime can be calculated as the sum of a lifetime due to the harmonic process and due to the impurities present in the system as indicated by Eq. 5.2:

$$\frac{1}{\tau} = \frac{1}{\tau_A} + \frac{1}{\tau_l} \tag{5.2}$$

where $\tau_A$ and $\tau_l$ are the decay times due to the harmonic process and the impurities present, respectively. Phonon lifetime can be calculated in terms of energy-time uncertainty using Eq. 5.3:

$$\frac{1}{\tau} = \frac{\Delta E}{\hbar} = 2\pi c\Gamma \tag{5.3}$$

where $\hbar$, $\Delta E$, c, and Γ are the reduced Planck constant, uncertainty in the phonon mode energy, velocity of light, and full width at half maximum obtained from Lorentzian fitting of Raman scattering curve, respectively. Sample 95Cu-5Zn showed the lowest phonon lifetime implying the decrease in electron-phonon coupling in this sample [50] Thus, the sample showed the highest photocurrent as will be shown later [51].

**Table 0.1**: Calculated phonon lifetime of the samples

| **Samples** | **Phonon Lifetime (ps)** |
|---|---|
| 95Cu-5Zn | 37.29 |
| 85Cu-15Zn | 38.15 |
| 70Cu-30Zn | 40.09 |
| 100Cu | 41.11 |

### 5.2.4 XPS results

X-ray photoelectron spectroscopy was conducted to determine the chemical composition of the as-anodized and as-annealed samples. The XPS spectra of the as-anodized

95Cu-5Zn sample are depicted in **Figure 5.8** a,b, and c, revealing the presence of $Cu^{+}$ at 931.96 eV and $Cu^{2+}$ at 934.36 eV. The spin-orbit splitting for Cu+ spectra is 19.9 eV, and 19.8 eV for $Cu^{2+}$. The peaks at 937.36, 941.16, and 960.16 eV are shake-up satellite peaks, which are characteristic of materials having $d^9$ configuration in the ground state such as CuO [52]. **Figure 5.8** b confirms the presence of Zn metal and $Zn^{2+}$ in the anodized 95Cu-5Zn sample. The peaks at 1021.68 and 1023.78 eV correspond to Zn metal and $Zn^{2+}$, respectively. The spin-orbit coupling for Zn metal is 23.3 eV and 23.6 eV for $Zn^{2+}$. **Figure 5.8** c shows the oxygen peaks, where the peaks at 529.48, 531.58, and 533.88 eV are attributed to oxygen in CuO lattice, ZnO lattice, and adsorbed water, respectively. **Figure 5.8** d,e,f reveals the changes that occurred to the samples after annealing. In **Figure 5.8** d, the sample is only composed of $Cu^{2+}$ in CuO with satellite peaks that correspond to CuO. Zn metal no longer exists in sample 95Cu-5Zn after annealing due to the high oxidation affinity of Zn, which is even higher than Cu, as shown in **Figure 5.8** [53]. **Figure 5.8** f shows that the amount of oxygen in the CuO lattice increased after annealing, as qualitatively proved, by the increase of the area under the graph of that peak. The amount of adsorbed water also decreased. Similar results were noted for the samples 85Cu-15Zn, 70 Cu-30Zn, 50 Cu-50Zn, and 100 Cu. It is worth noting that, even though ZnO peaks were not observed in XRD and Raman, there are peaks for $Zn^{2+}$ and O in the ZnO lattice in XPS. This is due to the fact that XRD and Raman are mainly bulk techniques, while XPS is a surface technique. Therefore, XPS was able to detect ZnO that formed on the outermost layer of the surface. It is well known that the annealing of α-brass leads to further oxidation of the surface. When oxidation proceeds at high temperatures, the Zn diffusion coefficient increases and Zn can diffuse through greater distances within a given time. The diffusion of Zn during the oxidation period thus proceeds directly from the bulk. The diffusion of Zn cation through the

outermost CuO-rich layer results in a p-type layer combined with Zn[54,55].

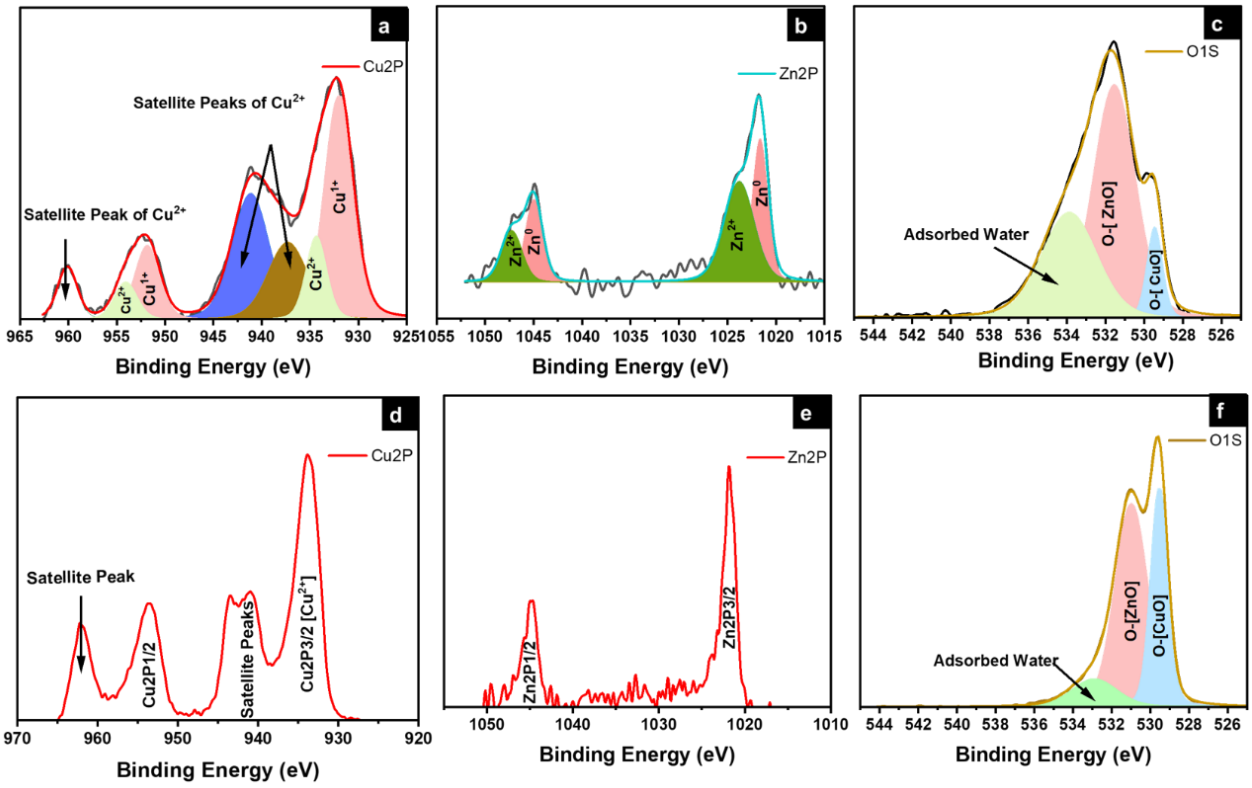


**Figure 5.8** High-resolution XPS spectra of the (a,b,c) as-anodized and (d,e,f) annealed 95Cu-5Zn sample.

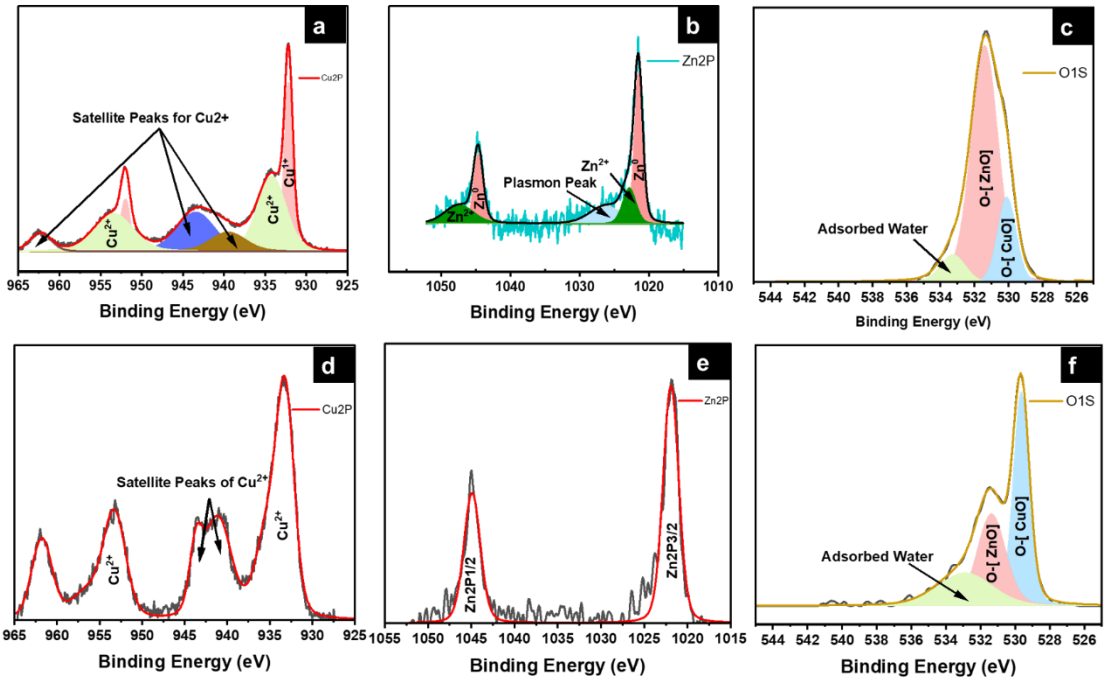


**Figure 5.9** High-resolution XPS spectra of the (a,b,c) as-anodized and (d,e,f) annealed 85Cu-15Zn sample.

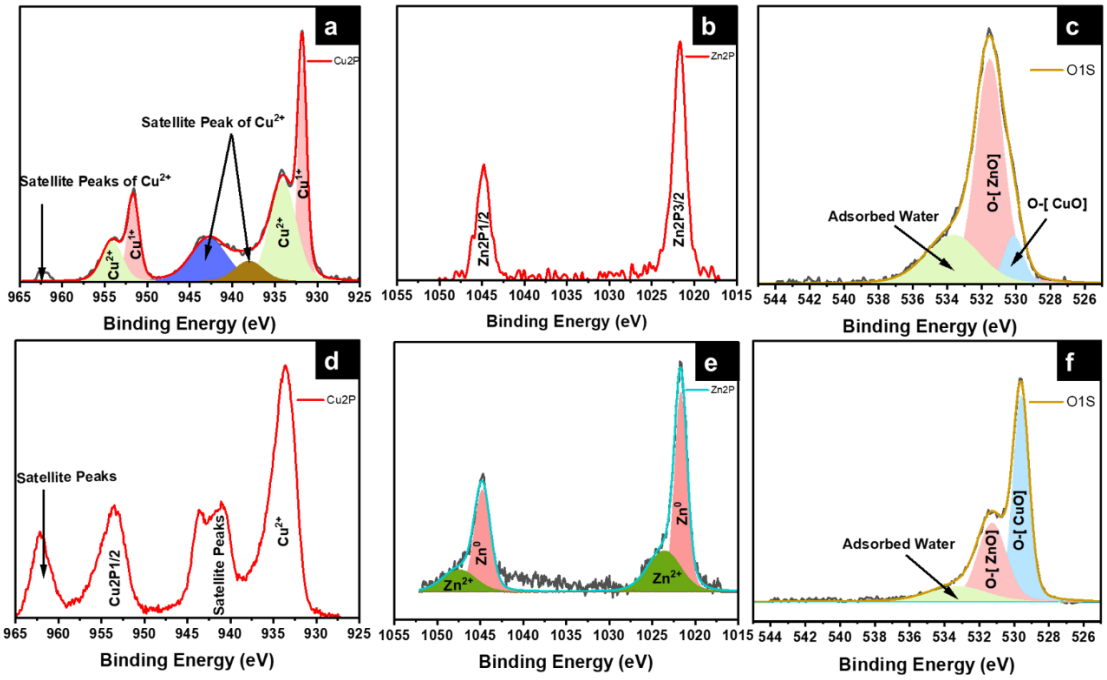


**Figure 5.10** High-resolution XPS spectra of the (a,b,c) as-anodized and (d,e,f) annealed 70Cu-30Zn.

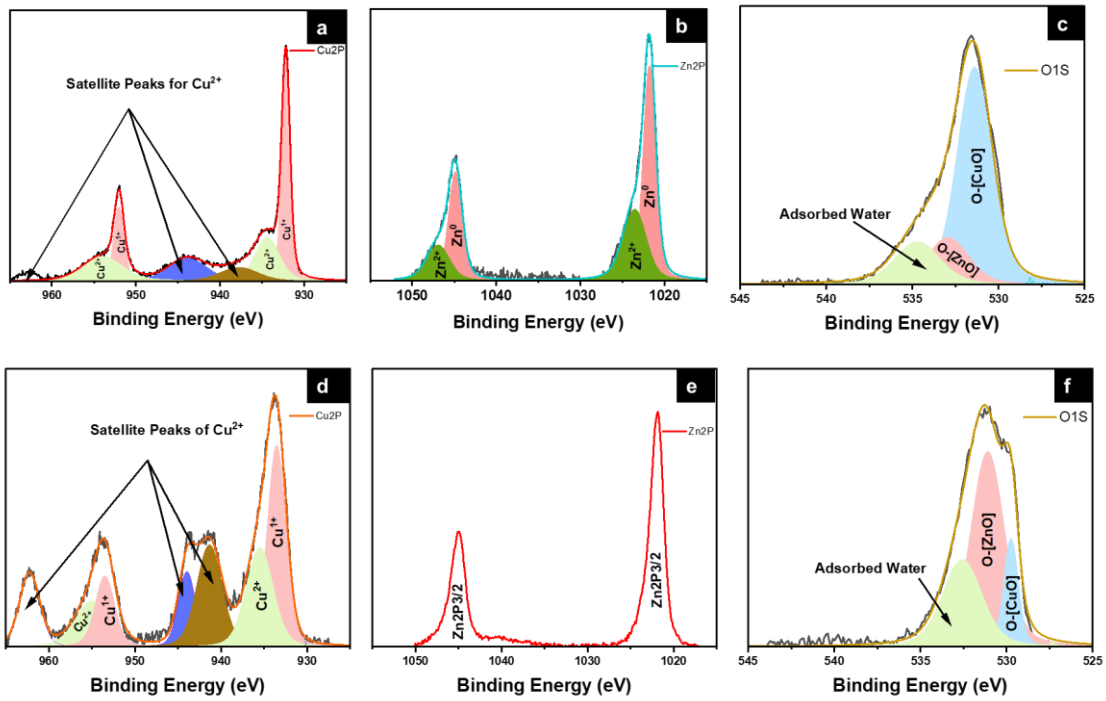


**Figure 5.11** High-resolution XPS spectra of the (a,b,c) as-anodized and (d,e,f) annealed 50Cu-50Zn sample.

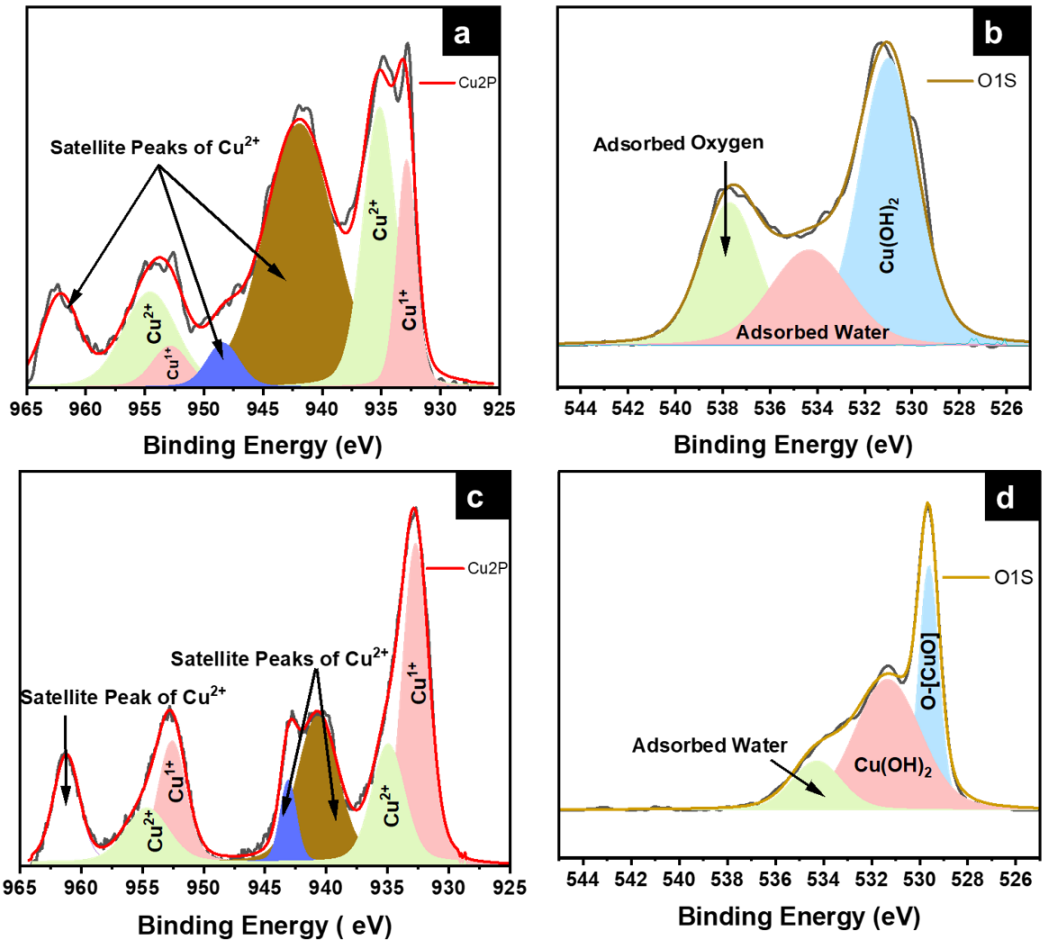


**Figure 5.12** High-resolution XPS spectra of the (a,b,c) as-anodized and (d,e,f) annealed 100 Cu sample.

Valence band XPS was conducted to determine the difference in Energy between the valence band maximum and the Fermi level, as shown in **Figure 5.13**

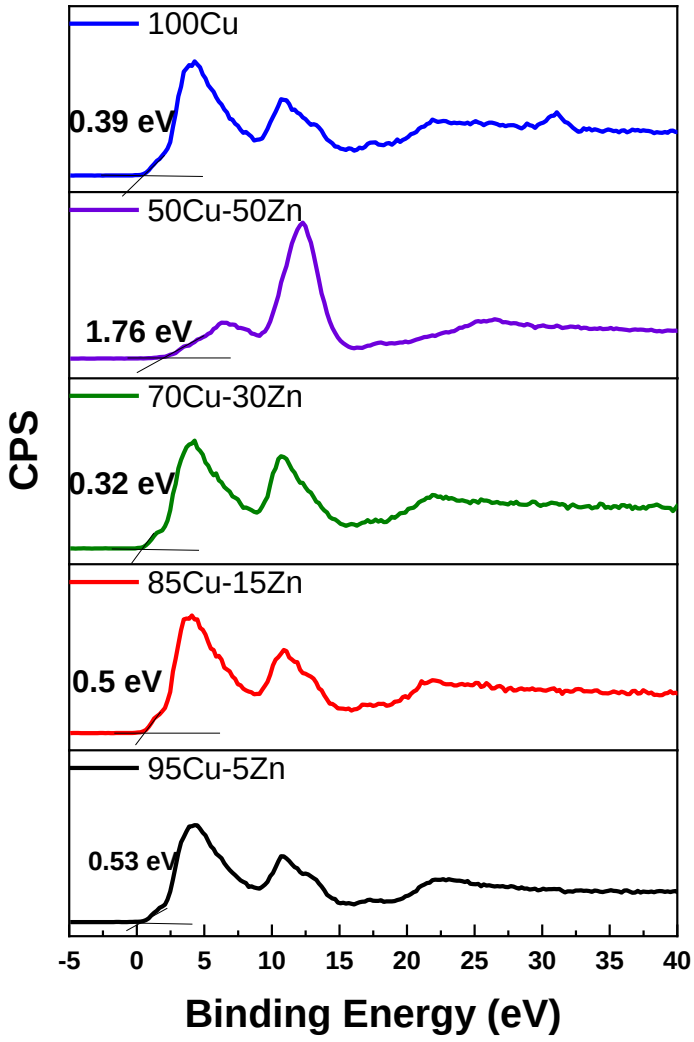


**Figure 5.13** Valence band XPS measurements for the samples.

### 5.2.5 UV-Vis absorbance measurements

Shimadzu UV–Vis diffuse reflectance spectrometer was used to study the optical properties of the samples, and the band gap of the samples was calculated using a Tauc plot, as shown in **Figure 5.14**, and **Figure 5.15**.

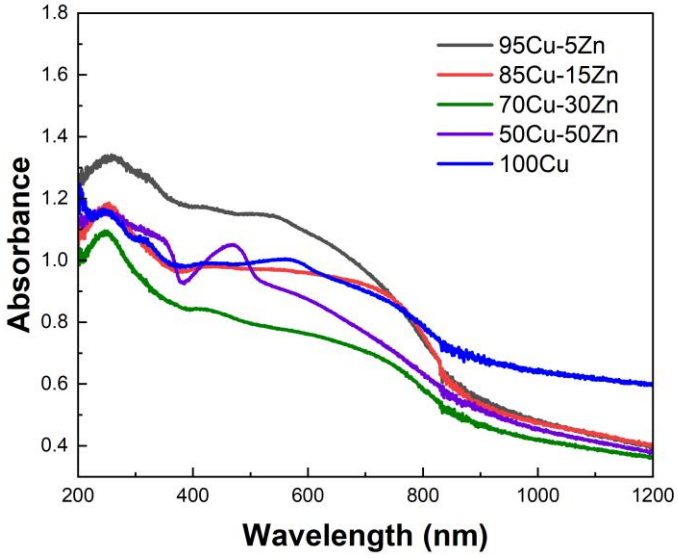


**Figure 5.14** Absorbance spectra for five annealed samples.

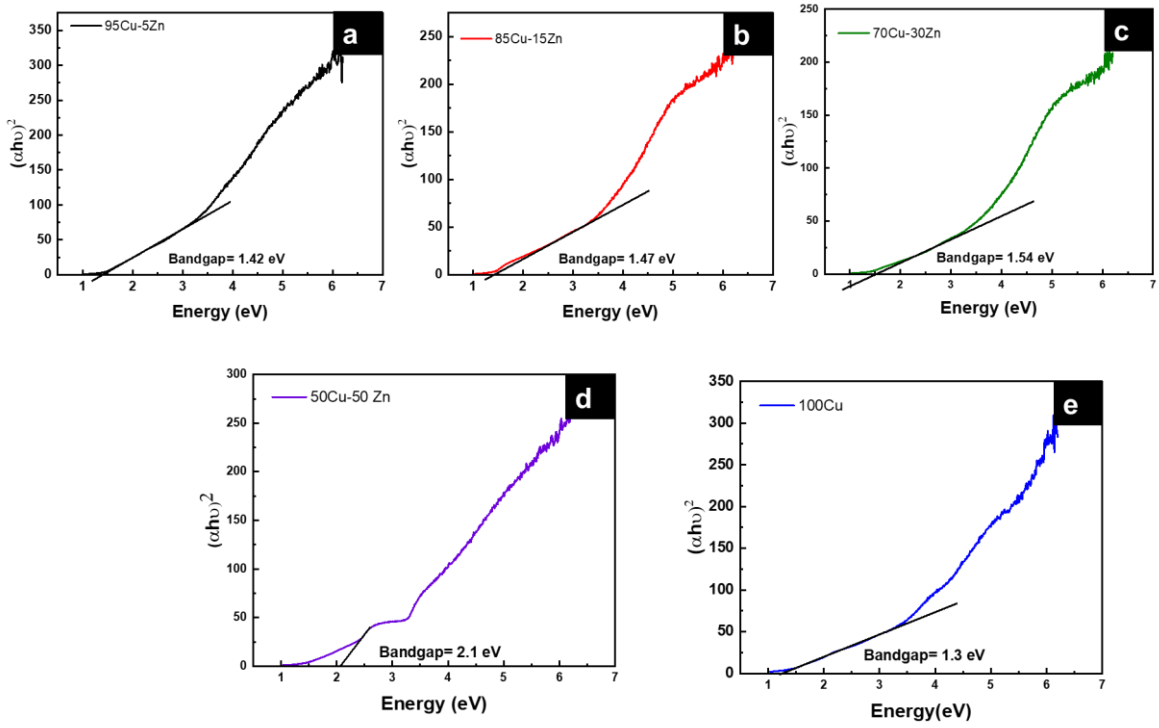


**Figure 5.15** Tauc plot and bandgap of the samples.

### 5.2.6 UPS results

UPS spectroscopy measurements help determine the electron affinity (χ) of the semiconductors according to Eq. 5.4:

$$\chi = h\nu - w - E_g \tag{5.4}$$

where χ is the electron affinity, $\boldsymbol{h\nu}$ is the excitation energy value of 21.2 eV used in UPS, $\boldsymbol{w}$ is a constant obtained by subtracting the secondary energy cutoffs obtained from the UPS spectra, and $\boldsymbol{E_g}$ is the bandgap of the material. **Figure 5.16** shows the UPS results for the samples.

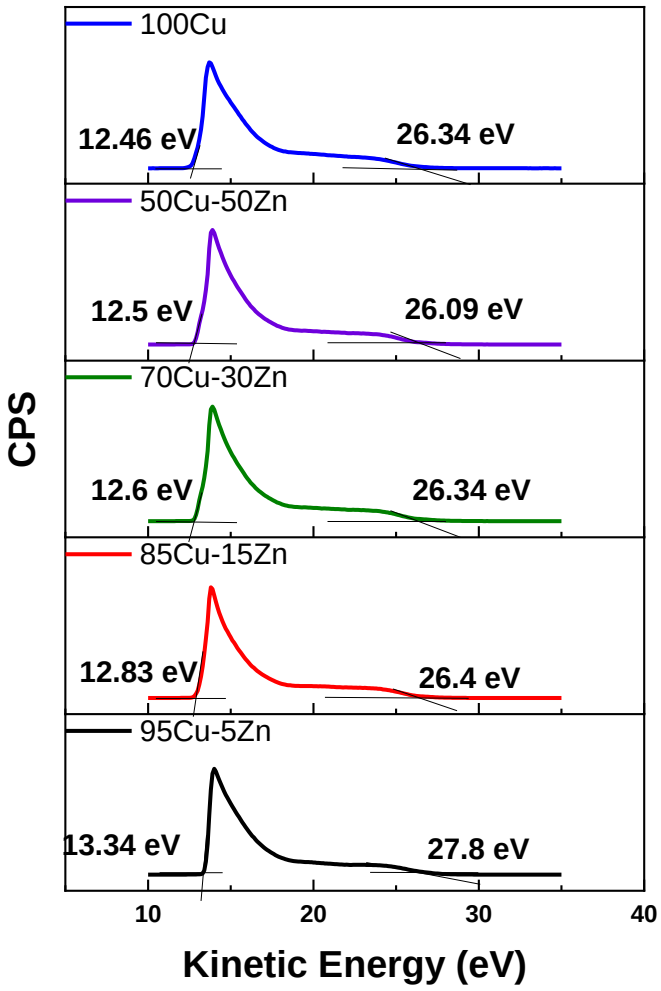


**Figure 5.16** UPS results for the samples .

The UV-Vis absorption spectra, Valence band XPS, and Ultraviolet Photoelectron Spectroscopy (UPS) measurements were carried out to determine the band positions of 95Cu-5Zn, 85Cu-15Zn, 70Cu-30Zn, 50Cu-50Zn, and 100Cu. The absorbance spectra can help determine the value of the optical bandgap of the sample using Tauc's plot calculations. Valence band XPS is a technique used to determine the energy difference between the valence band maximum position and the Fermi level position. The three measurements can be combined to determine the band positions of the samples with respect to vacuum energy levels. The band positions in **Figure 5.17** indicate that the conduction band position of all the samples is more positive than the hydrogen

evolution reaction potential, implying that the samples are suitable for water reduction. However, the valence band edge of the samples lies above the water oxidation potential, showing that the samples are not suitable for overall photoelectrochemical water splitting. Therefore, a photoanode needs to be used to create a tandem cell. The p-type behavior of the sample is evident, as the Fermi level ($E_f$) of the samples lies close to the valence band, which agrees well with the DFT calculations and Mott-Schottky measurements, as will be illustrated later.

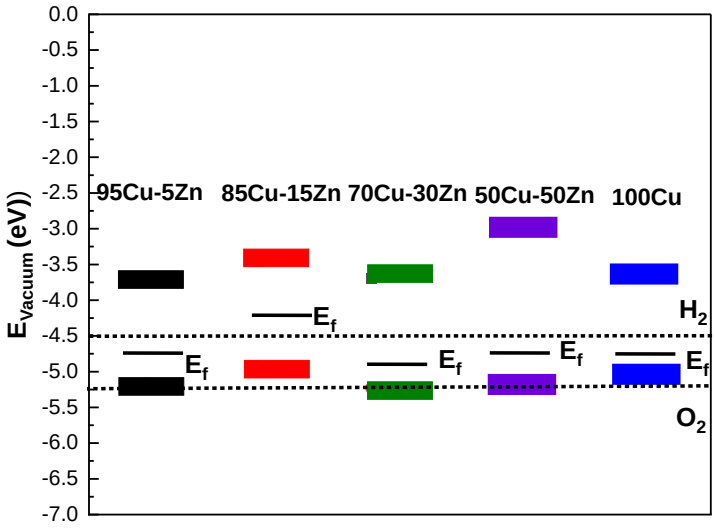


**Figure 5.17** Band edge positions of the samples.

## 5.3 Computational results

The electronic properties of the CuZnO (95%Cu, 5%Zn) material were investigated to gain a better understanding of its potential use in photoelectrochemical water splitting. The calculated electronic band structure (EBS) allows the estimation of the band gap energy and determination of the semiconductor type. The EBS calculation revealed a band gap of 1.445 eV and a shift of the Fermi level towards the valence band, as shown in **Figure 5.18 (b)** indicating a p-type semiconducting behavior. Additionally, the partial density of states (PDOS) was computed to provide statistical insights into the role of each orbital in the number of occupied

and unoccupied states as shown in **Figure 5.18 (c)** . While the region with low energy on the left side of the Fermi level represents the valence band, the region on the right represents the conduction band. Most of the state of the d orbital could be found in the valence band, which supports the hypothesis that the sample has a p-type semiconducting behavior. CuO is a p-type semiconductor with an indirect band gap of 1.44 eV [56].

The band gap of CuO determines its electronic and optical properties and is an important characteristic for its potential application in optoelectronic devices.[5] In our study, it was found that the band gap of CuO increased to 1.42 eV (experimentally), and 1.44 (computationally) due to the added Zn to the material. Specifically, the Zn d orbitals caused a slight shift in the energy of the conduction band away from the Fermi level, leading to a widening of the band gap. This finding could have implications for the development and optimization of CuO-based materials. Since the CuZnO structure is intended for use in photoelectrochemical water splitting, it is important to investigate its interaction with electromagnetic waves, specifically in the visible light region. The complex dielectric constant ε(ω) is a key factor in understanding this interaction. By analyzing the complex dielectric constant ε(ω) insights, the behavior of the CuZnO structure under different electromagnetic conditions can be obtained. Overall, these investigations into the electronic properties and electromagnetic interaction of the CuZnO structure provide a foundation for its potential use in PEC. In Eq. 1, the real and imaginary parts of the dielectric constant represent the energy gain and energy loss by the material, respectively. Through Eq.1, the dielectric constant was computationally found to be 2.26. The dielectric function of CuZnO is shown in Figure 5.19.

$$\varepsilon(\omega) = \varepsilon_1(\omega) + i\varepsilon_2(\omega) \quad (5.4)$$

The adsorption of hydrogen on the surface of the catalysts is a major step in the hydrogen evolution reaction (HER)[57]. HER is a two-electron transfer process with one catalytic

intermediate, H*. HER occurs through two individual steps, either the Volmer-Heyrovsky step or the Volmer-Tafel step. If the surface coverage of H* is low, the Heyrovsky reaction would be favored. If the surface coverage of H* is high, the Tafel reaction would be favored [58].

(Volmer reaction): $H^+ + e^- \rightarrow H^*$

(Tafel reaction): $2H^* \rightarrow H_2$

(Heyrovsky reaction): $H^* + H^+ + e^- \rightarrow H_2$

The energy of hydrogen adsorption ($E_{ads}$) is an important parameter in HER. A negative value means that $H^*$ binds favorably on the electrode surface making the Volmer reaction easy. However, if the value of adsorption energy is too negative, the next Tafel or Heyrovsky step would be difficult.[59] To study the catalytic activity of a CuZnO surface towards HER, it is important to identify the most favorable adsorption site for hydrogen on the surface of the catalyst. In this study, the adsorption energy of hydrogen on the Cu and Zn atoms of the CuZnO catalyst was calculated as:

$$E_{ads} = E_{H+surface} - E_{surface} - \frac{1}{2}E_{H_2} \quad (5.5)$$

where $E_{H+surface}$ is the total energy of the hydrogen atom on the surface, $E_{surface}$ is the total energy for the (-1 1 1) surface, and $E_{H_2}$ is the energy of the hydrogen molecule in a vacuum. The calculations showed that the adsorption energy of $H^*$ on the Cu atom is lower than that on the Zn atom. This indicates that the adsorption of $H^*$ on the Cu atom is more favorable than that on the Zn as illustrated in **Figure 5.18 (d)**. The low $E_{ads}$ on the Cu atom can block the desorption of $H_2$ molecules [60]. Therefore, substituting zinc atoms in the cupric oxide lattice leads to increasing the value of $E_{ads}$, implying that hydrogen will easily adsorb and desorb in the case of CuZnO structure more than mere CuO.

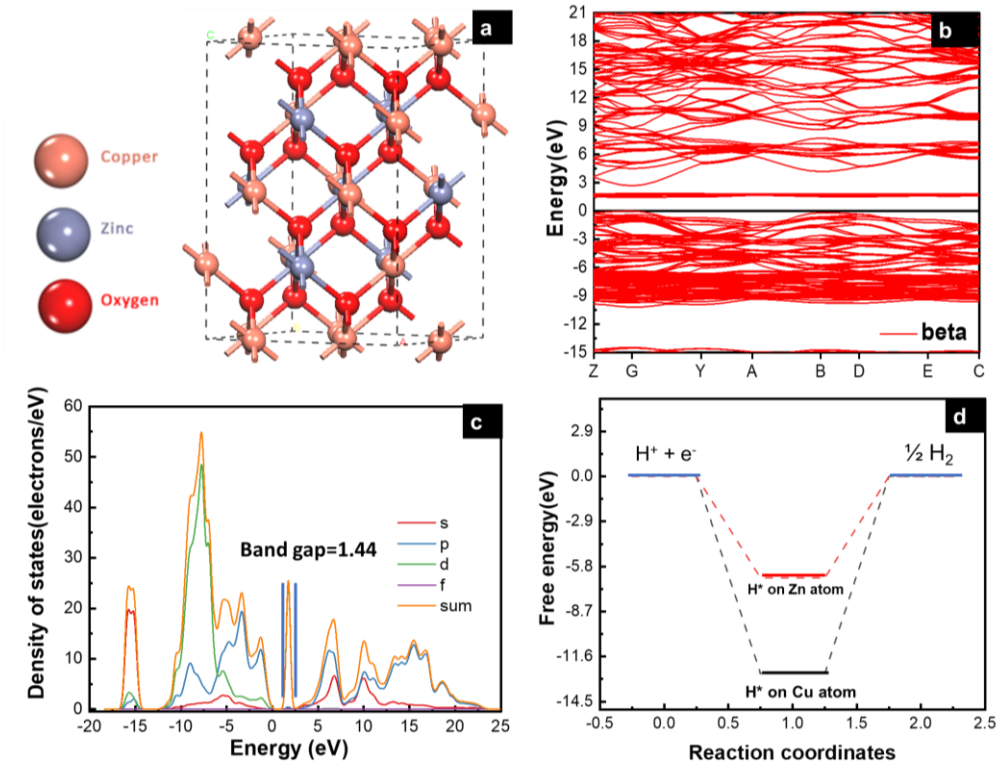


**Figure 5.18** (a) Side-view of CuZnO bulk (95%Cu,5%Zn), (b) electronic band structure specified by the Fermi level with black line, (c) partial density of states (PDOS), and (d) Free energy (eV) of H* adsorption on Cu and Zn atom.

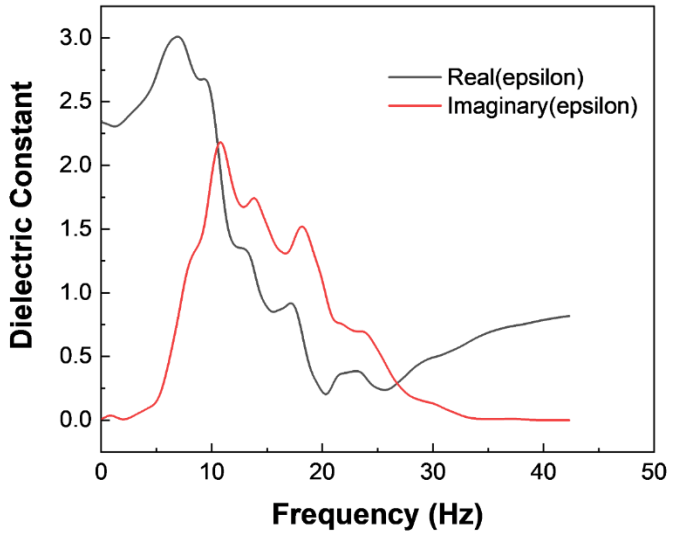


**Figure 5.19** Dielectric Function of CuZnO.

# Chapter 6

# Results and Discussion

# (Photoelectrochemical Measurements)

Herein, I report the photoelectrochemical measurements analysis of the fabricated nanostructured samples for their use as an attractive material for visible-light-driven photoelectrochemical water splitting. The photoelectrochemical performance was investigated in 0.1 M sodium carbonate (pH= 11.7) in a three-electrode system where Pt is the counter electrode, Hg/HgO is the reference electrode, and the fabricated nanostructured samples are the working electrode. We started with open circuit voltage measurements followed by LSV measurements, chopped illumination and continuous illumination CA measurements, EIS measurements under dark and light conditions, and Mott-Schottky measurements.

## 6.1 Open Circuit Voltage (OCV) measurements

OCV graph under switching (light on & off) conditions gives insight into the photovoltage of the samples. Sample 95Cu-5Zn shows the highest photovoltage change of 120 mV meaning that there will be a greater accumulation of photogenerated charge carriers, as shown in **Figure 6.1**. The recovery behavior of the photovoltage, when the light is terminated, can be due to the trapping and recombination of charge carriers mediated by trap states [61]. The photovoltage decay behaviors of the different samples, while the light is off, can be further utilized to calculate the decay lifetime by fitting the behavior to a biexponential function with two-time constants, as shown in Eq 6.1 and Eq 6.2

$$y(t) = A_0 + A_1 e^{-t/\tau 1} + A_2 e^{-t/\tau 2} \quad (6.1)$$

$$\tau_m = \frac{\tau_1 \tau_2}{\tau_1 + \tau_2} \quad (6.2)$$

where $\tau_1$ and $\tau_2$ are two relaxation time constants, representing two different recombination mechanisms during the decay process. The first represents the defect-related recombination at the surface, while the latter represents the band-to-band recombination in the bulk. t is the time and is the photovoltage at the beginning. and are two factors related to different recombination mechanisms. is the harmonic mean lifetime and log ($2\tau_m$) is the total half-life. The total half-life of the samples was calculated, as shown in **Table 1**. Sample 95Cu-5Zn showed the least decay lifetime implying that it has the least trap states.

**Table 6.1**: The calculated decay lifetime of the tested samples

| Samples | Total half-life (s) |
|---|---|
| 95Cu-5Zn | 0.34 |
| 85Cu-15Zn | 0.56 |
| 70Cu-30Zn | 0.44 |
| 50Cu-50Zn | 0.67 |

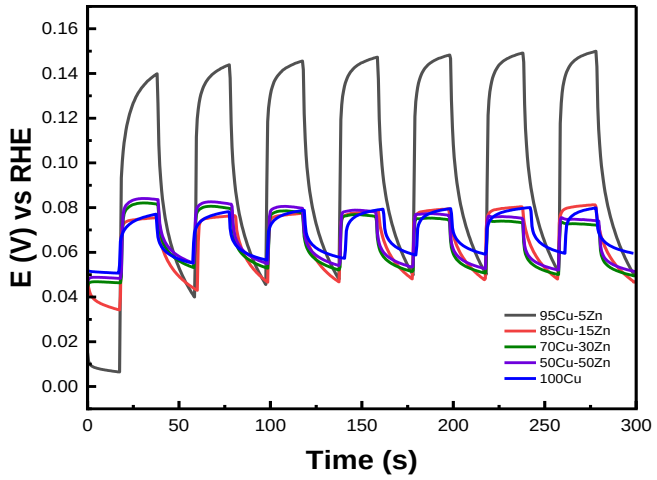


**Figure 6.1** Open circuit voltage as the illumination is chopped(pH= 11.7, $NaCO_3$ electrolyte)..

## 6.2 Cyclic Voltammetry (CV)

The photoelectrochemical measurements were performed to assess the performance of the material for photoelectrochemical water reduction. The cyclic voltammetry (CV) was first recorded to evaluate the stability of the photocathode in the electrolyte while performing a cathodic sweep, **Figure 6.2**. The first reduction peak is attributed to $Cu^{2+}$ reduction to $Cu^{+}$ and the second reduction peak is attributed to the reduction of $Cu^{+}$ to $Cu^{0}$ [26,62]. The intensity of the two reduction peaks decreased for the Zn-alloyed samples, proving that zinc alloying reduces the reduction of copper. When there is a high barrier to electron transfer, the electron transfer reactions are sluggish, therefore more negative potential is needed to observe reduction. As shown in Figure 6.2 , alloying Cu with zinc gives rise to larger ΔEp meaning that the reduction of copper has become more sluggish, upon alloying with zinc, which is more beneficial in the PEC system in our study.

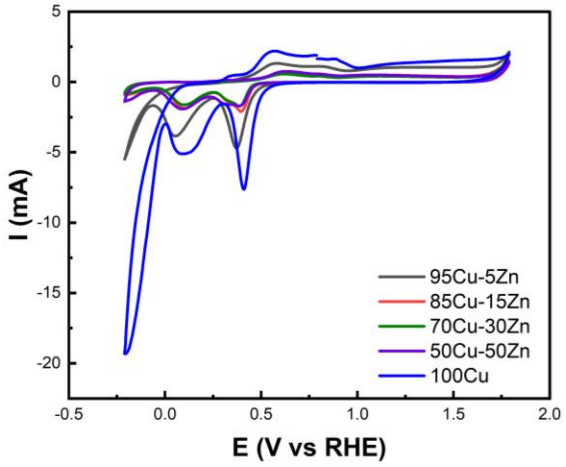


**Figure 6.2** Cyclic voltammetry measurements of the samples (pH= 11.7, $NaCO_3$ electrolyte). .

## 6.2 Linear Sweep Voltammetry (LSV) measurements

LSV was performed to scan the photocurrent of the samples under dark and illumination conditions versus applied voltage. Even though the 100Cu sample shows the highest photocurrent density under illumination followed by the 95Cu-5Zn sample, the dark current density of the 100Cu sample was the highest, as shown in **Figure 6.3**. That is why we take into consideration the difference between the dark current density and the photocurrent under illumination to judge the best sample in terms of photocurrent density. The photocurrent density of each sample is illustrated in **Table 2**.

**Table 6.2**: Photocurrent density of the tested samples.

| **Samples** | **Photocurrent Density ($mA/cm^2$)** |
|---|---|
| 95Cu-5Zn | 0.26 |
| 85Cu-15Zn | 0.124 |
| 70Cu-30Zn | 0.137 |

| | |
|---|---|
| 50Cu-50Zn | 0.1 |
| 100Cu | 0.17 |

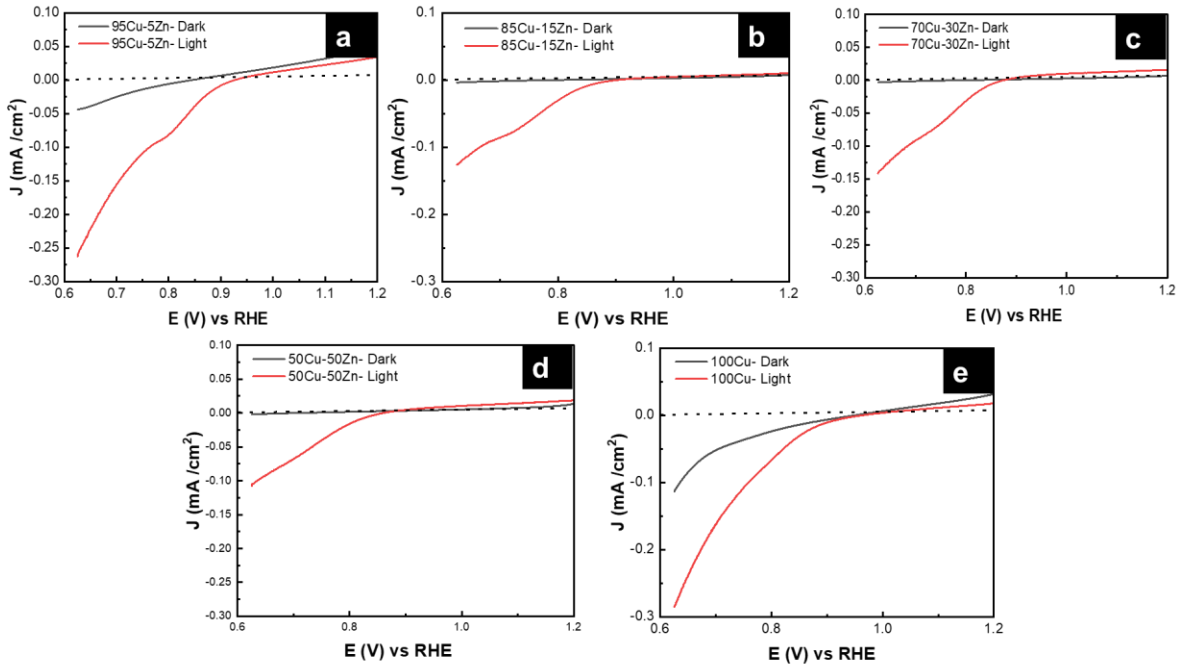


**Figure 6.3** Linear sweep voltammetry (LSV) graphs for (a) 95Cu-5Zn, (b) 85Cu-15Zn, (c) 70Cu-30Zn, (d) 50Cu-50Zn, and (e) 100 Cu (pH= 11.7, $NaCO_3$ electrolyte).

## 6.3 Chronoamperometry (CA) measurements

Chronoamperometry was conducted to test the stability of the sample under chopped illumination. The initial spike upon light illumination is attributed to the rapid separation of photogenerated charge carriers in the space charge region, with electrons moving to the interface to charge the space charge capacitance and holes passing to the external circuit for p-type semiconductors. The following photocurrent decay is attributed to the accumulation of minority charge carriers (electrons) at the interface causing an increase in the flow of holes due to recombination. Then, a steady state is reached. The positive overshoot observed when the light

is switched off is because the electron flux is interrupted revealing the mere hole flux [63]. From the current-time graph, we were able to calculate the transient time constant. **Figure 6.4**shows J-t curves for the samples. The J-t curves enabled us to calculate the transient time constant, as shown in Table 3. The immediate photoresponse ($I_{in}$) is followed by an exponential decrease of the photocurrent until a stationary value is reached ($I_{st}$). A ratio (R) that correlates between the ($I_{in}$) and ($I_{st}$) is defined based on Eq. 6.3:

$$R = \frac{I_t - I_{st}}{I_{in} - I_{st}} \tag{6.3}$$

where $I_t$ is current at time $t$, the photocurrent transient can be described by Eq. 6.4:

$$R = e^{-t/\tau} \tag{6.4}$$

where $\tau$ is the transient time constant. Therefore, the slope of ln(R) *vs* time is the reciprocal of $\tau$.

It is worth mentioning that as the transient time constant increases, the recombination process gets delayed, as the charge carriers keep their excitation at the SEI for longer times. Sample 95Cu-5Zn shows the highest transient time constant compared to other counterparts. Therefore, the photogenerated electrons will have more time to transfer to the interface initiating the water reduction reaction[64,65]. To elucidate the role of Zn on the stability of the 95Cu-5Zn sample, we have performed a chronoamperometric long-term stability test under constant illumination for four hours, as shown in **Figure 6.5**.

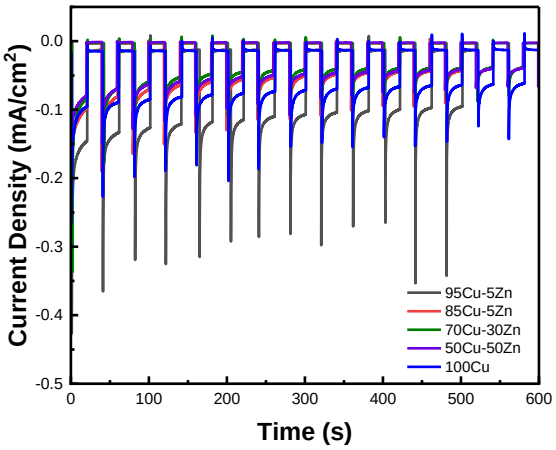


**Figure 6.4** Chronoamperometry graphs for five samples (pH= 11.7, $NaCO_3$ electrolyte, voltage =0.62 V vs RHE).

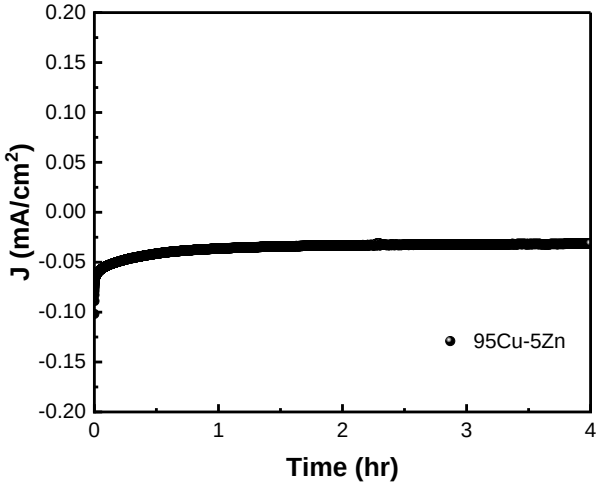


**Figure 6.5** Chronoamperometry graph for sample 95Cu-5Zn under constant illumination for four hours, voltage = 0.62 V vs RHE.

**Table 6.3**: Transient time constant measurements.

| **Samples** | **Transient time constant (s)** |
|---|---|
| 95Cu-5Zn | 5.78 |

| | |
|---|---|
| 85Cu-15Zn | 5.03 |
| 70Cu-30Zn | 5.128 |
| 50Cu-50Zn | 5.36 |

Through chronoamperometry measurements, we were able to calculate the retention current, as shown in Table 4. It is worth noting that sample 100 Cu was exempted from the retention current calculations, transient time constant calculations, transient photovoltage calculations, long term stability measurements, and electrochemical impedance spectroscopy measurements, since the photocurrent results in cupric oxide reduction rather than hydrogen evolution, as will be shown by hydrogen quantification measurements. Sample 95Cu-5Zn shows the highest retention current proving that the addition of Zn up to 5% has improved the stability of the sample.

$$Retention\ \% = \frac{I_{500}}{I_0} * 100$$

where $I_{500}$ is the current at 500 s, and $I_0$ is the initial current.

**Table 6.4**: The calculated retention current for the tested samples

| **Samples** | **Retention Current (%)** |
|---|---|
| 95Cu-5Zn | 66.53 |
| 85Cu-15Zn | 42.76 |
| 70Cu-30Zn | 46.93 |
| 50Cu-50Zn | 45.92 |

## 6.4 Electrochemical Impedance Spectroscopy (EIS) measurements

EIS measurements were conducted to reveal the interfacial interactions of the samples in the dark and under simulated sunlight illumination at an applied potential of 0.62 V vs RHE. Preceding studies only revealed the role of SCL in transferring the electrons from the bulk of the semiconductor to the electrolyte. However, a few studies showed the role of surface states for Cu-based photocathodes; illustrating their chemical capacitance related to the accumulation/transfer of charge through potential surface states at low frequencies. In this study, we propose using an equivalent circuit (EC) that considers the probable surface states to fit EIS data. The equivalent circuit is shown in Figure 6.5. The EIS Data under dark and illumination conditions are shown in **Figure 6.6**. Two semicircles can be observed for each sample as shown in **Figure 6.7** and they are shown at the inset of the figure. EIS data under illumination are shown in **Figure 6.7 b**. Illumination induces a decrease in the radius of the semicircle in Nyquist plot indicating a lower value of overall resistance due to the photoconductivity of all samples. It is also observed that sample 95Cu-5Zn has the lowest total resistance [66].

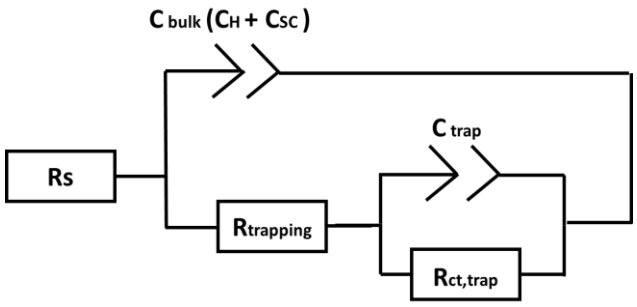


**Figure 6.6** Equivalent circuit for electrochemical impedance spectroscopy data fitting.

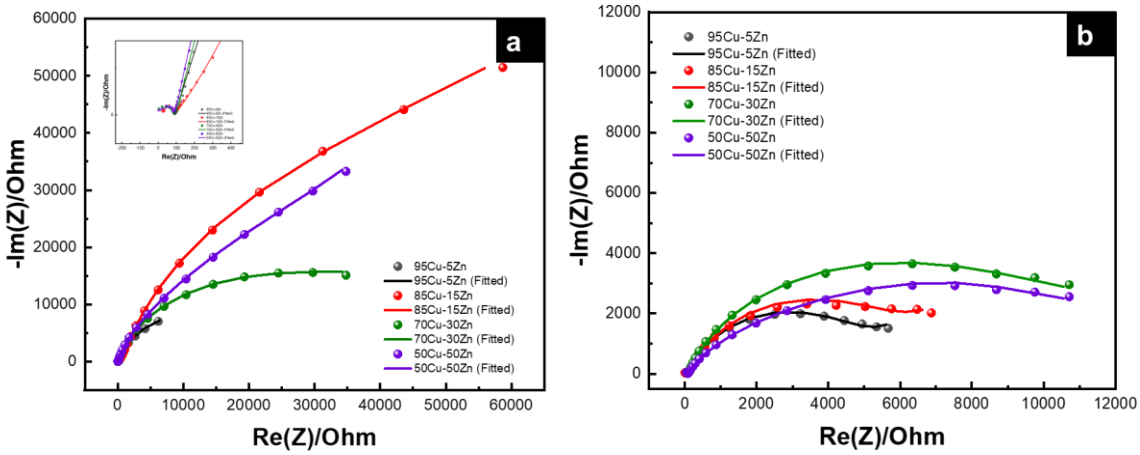


**Figure 6.7** EIS data for Cu-Zn samples under (a) Dark and (b) light conditions (pH= 11.7, $NaCO_3$ electrolyte, voltage =0.62 V vs RHE)

To get more insight into the trapping of charges on the surface and to prove the existence of surface states, $C_{trap}$ values at low frequencies are shown in **Figure 6.8 and Figure 6.9.** The low frequency guarantees the low contribution of $C_{bulk.}$ Therefore, we have chosen the frequency of 50 mHz to get the value of $C_{trap}$ versus applied potential. In the dark and under illumination, $C_{trap}$ shows a Gaussian peak for all samples shown through the fitting of the sample to a Gaussian function, which is a proof of the existence of surface states at around 0.8 V vs RHE.

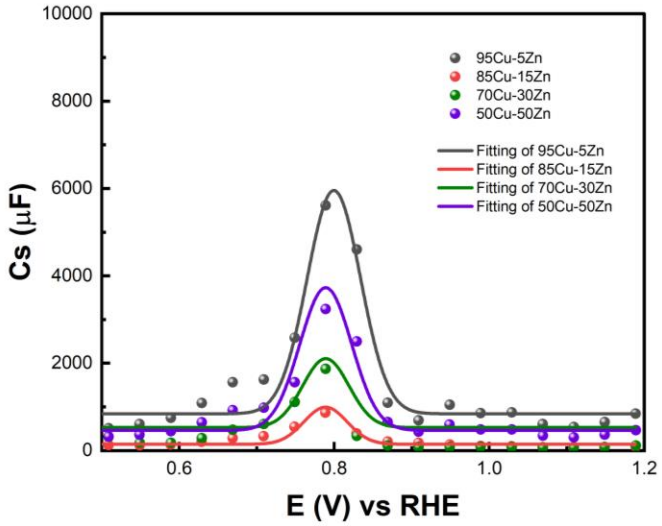


**Figure 6.8** $C_{trap}$ versus applied potential for the samples at 50 mHz under dark conditions (pH= 11.7, $NaCO_3$ electrolyte, voltage =0.62 V vs RHE).

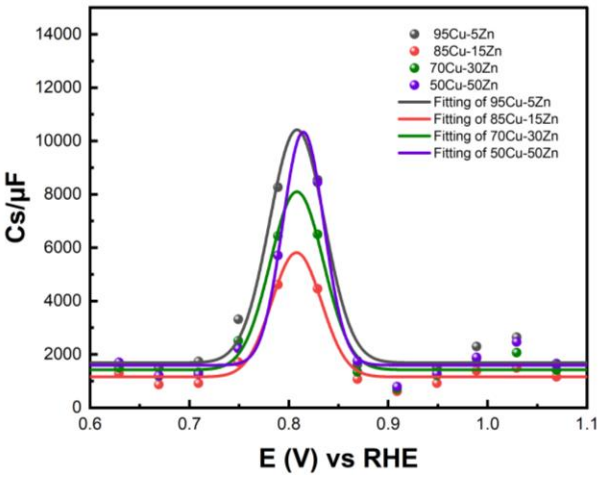


**Figure 6.9** $C_{trap}$ versus applied potential for the samples at 50 mHz under illumination conditions (pH= 11.7, $NaCO_3$ electrolyte, voltage =0.62 V vs RHE).

### 6.5 Mott Schottky Measurements

To study the relationship between the space charge layer capacitance $C_{sc}$, the acceptor density ($N_A$), the applied potential V , and the flat band potential ($V_{FB}$) , Mott-Schottky measurements were conducted in the dark , as shown in **Figure 6.10**. The negative slopes of the plots indicate the p-type nature of the samples. Charge carrier density was calculated

using Eq. 6.4:

$$\frac{1}{Csc^2} = \left(\frac{2}{e\epsilon\epsilon_0 N_A}\right)\left[V - V_{FB} - \frac{K_B T}{e}\right] \quad (6.4)$$

where $e$ is the electronic charge, $\epsilon$ is the dielectric constant, $\epsilon_0$ is the vacuum permittivity, $V_{FB}$is the flat-band potential of the electrode, $K_B$ is Boltzmann constant, and $T$ is the temperature in Kelvin. The calculated charge carrier density and flatband potential are shown in **Table 5**. Moreover, M-S measurements helped with determining the band positions of the samples, which was in a qualitatively good agreement with the UPS measurements showing that the samples straddle the HER. Sample 95Cu-5Zn showed the highest charge carrier density, which might be the reason why it showed the highest photocurrent and the best performance among the samples, as shown in **Figure 6.11** .

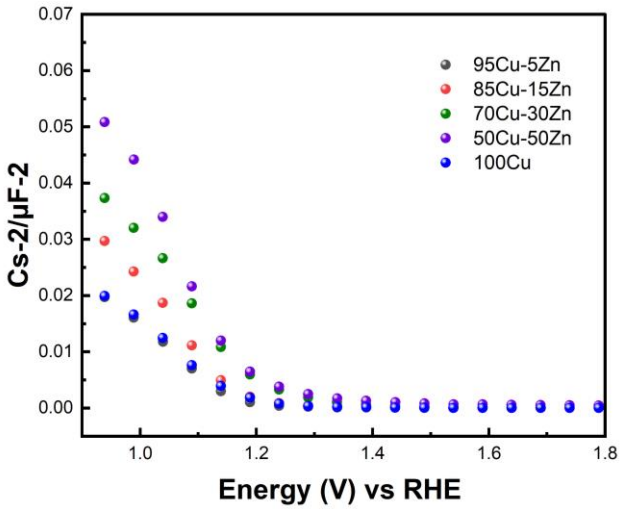


Figure 6.10 M-S plots of the samples (pH= 11.7, $NaCO_3$ electrolyte)

**Table 6.5**: Mott- Schottky Analysis results of the samples

| Samples | $V_{FB}$ (V vs RHE) | $N_a$ ($cm^{-3}$) |
|---|---|---|
| | | |

| | | |
|---|---|---|
| 95Cu-5Zn | 1.150 | $6.202 \times 10^{20}$ |
| 85Cu-15Zn | 1.169 | $4.531 \times 10^{20}$ |
| 70Cu-30Zn | 1.203 | $3.977 \times 10^{20}$ |
| 50Cu-50Zn | 1.190 | $2.854 \times 10^{20}$ |
| 100Cu | 1.156 | $6.133 \times 10^{20}$ |

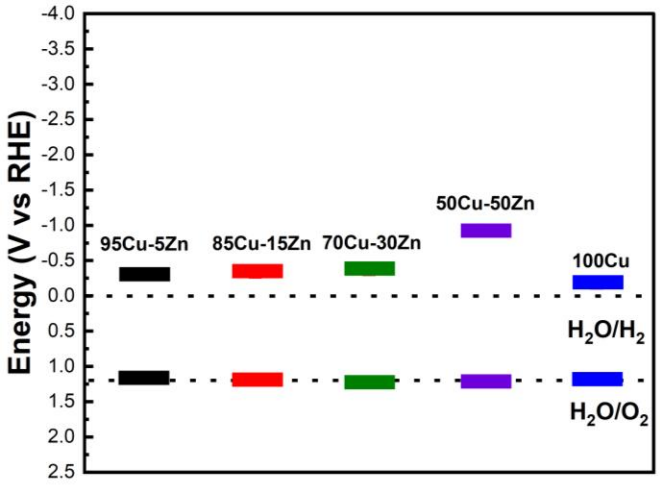


**Figure 6.11** Band positions of the samples using M-S measurements.

## 6.6 Hydrogen Quantification

The main challenge in using CuO-based photocathodes is ensuring that the photocurrent produced results from HER and not from the self-reduction of the photocathode. Therefore, quantifying the amount of hydrogen produced is of paramount importance to ensure that the photocurrent is mainly from hydrogen production. In this regard, the 95Cu-5Zn sample showed an amount of hydrogen of 0.2658 µmole after 60 minutes of continuous illumination, as shown in Figure 6.9. However, the 100 Cu sample only showed 3.965 nmole after 20 minutes of illumination. After 20 minutes, it was observed that the sample was covered with a very

shiny metal surface covering the area exposed to the light. These findings mean that most of the photocurrent resulting from the 100Cu sample in our chronoamperometry studies is due to the photoreduction of cupric oxide to copper and not from hydrogen production. Therefore, we can conclude that alloying CuO with 5% Zn leads to improving the stability of the material in PEC application. **Table 6.6** shows where our results stand among other copper-based photocathodes.

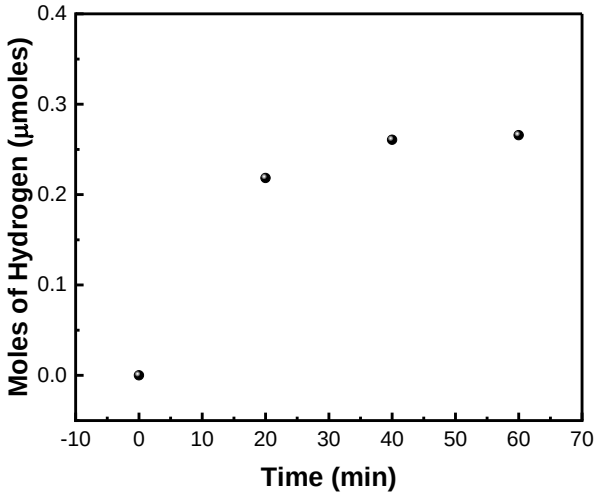


**Figure 6.12** Hydrogen Quantification of the 95Cu-5Zn Sample

**Table 6.5**: Mott- Schottky Analysis results of the samples

| **Photocathode** | **Experimental Conditions** | **Amount of Hydrogen evolved** |
|---|---|---|
| $CuFe_xO_y$ [67] | Applying constant current of 10μA | 4.8 nmol $cm^{-2}$ (after one hour of continuous illumination) |
| Carbon coated $Cu_2O$ nanowires [68] | Applying a constant voltage of 0V vs RHE | ~ 6 μmol $cm^{-2}$ (after 16.6 mins of continuous illumination) |
| Li incorporated in $CuAl_2O_4$ [69] | Applying a constant voltage of 0.4V vs RHE | ~ 0.27 μmol $cm^{-2}$ (after one hour of continuous illumination) |
| Li doped CuO[70] | Applying a constant voltage of 0.3 V vs RHE | ~ 0.2 nmol $L^{-1}$ (after 15 minutes of continuous illumination) |
| **This work** | **Applying a constant voltage of 0.6 V vs RHE** | **1.06 μmol $cm^{-2}$ (after one hour of continuous illumination)** |

# Chapter 7

# Conclusion and Future Work

## 7.1 Conclusion

Considering the development of renewable energy sources is of paramount importance to the future of our planet. Among the current available technologies is the green hydrogen production through water splitting. Currently, the industry relies on the electrolysis of water for the production of green hydrogen. However, the use of solar light can make us rely less on electricity and reduce the cost. This thesis has covered an experimental based framework to analyze and validate the usage of p-type photoelectrodes in photoelectrochemical water splitting for green hydrogen production. However, the core challenge associated with scaling up photoelectrochemical water splitting using photocathodes is the fact that photocathodes are not stable when in direct contact with an electrolyte. In this thesis, we report Cu-Zn based nanostructures for efficient green hydrogen production. The following conclusions are drawn:

- Starting with anodization and annealing of the brass alloy leads to the formation of homogenously distributed nanostructures over the metal alloy.
- Varying the content of Zn leads to changing the physical and chemical properties of the samples when compared to a sample consisting of 100% Cu.
- Cu-Zn based electrodes have conduction band edges that are more negative than HER making them good candidates for water reduction reaction.
- Upon the use of the samples as photoelectrodes to split water under AM 1.5 illumination, the sample that contains 5% zinc showed a photocurrent density of -0.26 $mA/cm^2$ at 0.62V vs RHE, a high long-term stability, a high charger carrier density , and low total resistance.

- The amount of hydrogen evolved upon the use of the 95Cu-5Zn photocathode was 0.2658 µmole after one hour of continuous illumination, while the 100Cu sample could barely withstand 20 minutes of illumination producing only 3.965 nmole of hydrogen before being completely reduced into Cu metal.

Finally, I hope those findings will inspire other researchers to implement the synthesized photoelectrodes in their work and work more towards the realization of scalable and stable photoelectrodes for their use in PEC.

### 7.2 Future Work

**Based on the discussion presented in Chapter 5 and Chapter 6:**

- A combination of other Cu-Zn based alloys with lower concentrations of Zn can be further explored to correlate the lower composition with the photocatalytic performance. This can be done through estimating the threshold concentration that will lead to a better activity.
- A detailed DFT study of the thermodynamic oxidation and reduction potentials of the Cu-Zn based alloys is of a great importance, as it will show whether the photocorrosion is reduced or not computationally.
- The addition of an n-type protective layer to the surface of the proposed photocathodes and the decoration of the surface with a co-catalyst might be of a great interest to increase the photocurrent and the hydrogen quantification.
- Coupling the proposed photocathode with an efficient photoanode can be an extensive study to test how the proposed photocathodes will perform in a PEC water splitting device.
- Investigating the photostability of the photocathodes at various temperatures can be of an interest to commercial and industrial applications.

# References


1. Bonds, E. Assessing the Oil Motive After the U.S. War in Iraq. *Peace Review* **25**, 291–298 (2013).
2. Guan, Y. *et al.* Burden of the global energy price crisis on households. *Nat Energy* **8**, 304–316 (2023).
3. Xu, J. *et al.* Energy crisis, firm profitability, and productivity: An emerging economy perspective. *Energy Strategy Reviews* **41**, 100849 (2022).
4. Karakurt, I. & Aydin, G. Development of regression models to forecast the CO2 emissions from fossil fuels in the BRICS and MINT countries. *Energy* **263**, 125650 (2023).
5. $CO_2$ and Greenhouse Gas Emissions. *Our World in Data* (2017).
6. Lindsey, R. Climate Change: Atmospheric Carbon Dioxide. *climate.gov* (2023).
7. Wijaya, A. S. Climate Change, Global Warming and Global Inequity in Developed and Developing Countries ( *Analytical Perspective, Issue, Problem and Solution)*. *IOP Conf Ser Earth Environ Sci* **19**, 012008 (2014).
8. Diffenbaugh, N. S. & Barnes, E. A. Data-driven predictions of the time remaining until critical global warming thresholds are reached. *Proceedings of the National Academy of Sciences* **120**, (2023).
9. Ang, T.-Z. *et al.* A comprehensive study of renewable energy sources: Classifications, challenges and suggestions. *Energy Strategy Reviews* **43**, 100939 (2022).
10. Younas, M., Shafique, S., Hafeez, A., Javed, F. & Rehman, F. An Overview of Hydrogen Production: Current Status, Potential, and Challenges. *Fuel* **316**, 123317 (2022).
11. DOE Technical Targets for Hydrogen Production from Photoelectrochemical Water Splitting. *Department of Energy* (2023).
12. Kannan, N. & Vakeesan, D. Solar energy for future world: - A review. *Renewable and Sustainable Energy Reviews* **62**, 1092–1105 (2016).
13. Beswick, R. R., Oliveira, A. M. & Yan, Y. Does the Green Hydrogen Economy Have a Water Problem? *ACS Energy Lett* **6**, 3167–3169 (2021).
14. Joy, J., Mathew, J. & George, S. C. Nanomaterials for photoelectrochemical water splitting – review. *Int J Hydrogen Energy* **43**, 4804–4817 (2018).
15. *Light, Water, Hydrogen*. (Springer US, 2008). doi:10.1007/978-0-387-68238-9.
16. Yang, X. & Wang, D. Photophysics and Photochemistry at the Semiconductor/Electrolyte Interface for Solar Water Splitting. in 47–80 (2017). doi:10.1016/bs.semsem.2017.03.001.
17. Tan, H. L., Abdi, F. F. & Ng, Y. H. Heterogeneous photocatalysts: an overview of classic and modern approaches for optical, electronic, and charge dynamics evaluation. *Chem Soc Rev* **48**, 1255–1271 (2019).
18. Khalaf, N., Abdel-Motalib, A. & Allam, N. K. *AN INVESTIGATION INTO THE DOPING AND CRYSTALLINITY OF ANODICALLY FABRICATED TiO 2 NANOTUBE ARRAYS: TOWARDS AN EFFICIENT MATERIAL FOR SOLAR ENERGY APPLICATIONS*. (2009).
19. *Electrochemical Methods*.

20. Kalanur, S. S., Duy, L. T. & Seo, H. Recent Progress in Photoelectrochemical Water Splitting Activity of WO3 Photoanodes. *Top Catal* **61**, 1043–1076 (2018).
21. Abdi, F. F., Gutierrez Perez, R. R. & Haussener, S. Mitigating voltage losses in photoelectrochemical cell scale-up. *Sustain Energy Fuels* **4**, 2734–2740 (2020).
22. Jang, Y. J. & Lee, J. S. Photoelectrochemical Water Splitting with p-Type Metal Oxide Semiconductor Photocathodes. *ChemSusChem* **12**, 1835–1845 (2019).
23. Chen, S. & Wang, L.-W. Thermodynamic Oxidation and Reduction Potentials of Photocatalytic Semiconductors in Aqueous Solution. *Chemistry of Materials* **24**, 3659–3666 (2012).
24. Govind Rajan, A., Martirez, J. M. P. & Carter, E. A. Why Do We Use the Materials and Operating Conditions We Use for Heterogeneous (Photo)Electrochemical Water Splitting? *ACS Catal* **10**, 11177–11234 (2020).
25. Li, C., He, J., Xiao, Y., Li, Y. & Delaunay, J.-J. Earth-abundant Cu-based metal oxide photocathodes for photoelectrochemical water splitting. *Energy Environ Sci* **13**, 3269–3306 (2020).
26. Li, Y. & Luo, K. Flexible cupric oxide photocathode with enhanced stability for renewable hydrogen energy production from solar water splitting. *RSC Adv* **9**, 8350–8354 (2019).
27. Cots, A., Bonete, P. & Gómez, R. Cupric oxide nanowire photocathodes stabilized by modification with aluminum. *J Alloys Compd* **867**, 158928 (2021).
28. Cots, A., Bonete, P. & Gómez, R. Improving the Stability and Efficiency of CuO Photocathodes for Solar Hydrogen Production through Modification with Iron. *ACS Appl Mater Interfaces* **10**, 26348–26356 (2018).
29. Oh, J., Ryu, H., Lee, W.-J. & Bae, J.-S. Improved photostability of a CuO photoelectrode with Ni-doped seed layer. *Ceram Int* **44**, 89–95 (2018).
30. Li, J. *et al.* Copper oxide nanowires for efficient photoelectrochemical water splitting. *Appl Catal B* **240**, 1–8 (2019).
31. Shaislamov, U. *et al.* Highly stable hierarchical p-CuO/ZnO nanorod/nanobranch photoelectrode for efficient solar energy conversion. *Int J Hydrogen Energy* **41**, 2253–2262 (2016).
32. Xing, H. *et al.* Exposing the photocorrosion mechanism and control strategies of a CuO photocathode. *Inorg Chem Front* **6**, 2488–2499 (2019).
33. Tilley, S. D. Will Cuprous Oxide Really Make It in Water-Splitting Applications? *ACS Energy Lett* **8**, 2338–2344 (2023).
34. Kunturu, P. P. & Huskens, J. Efficient Solar Water Splitting Photocathodes Comprising a Copper Oxide Heterostructure Protected by a Thin Carbon Layer. *ACS Appl Energy Mater* **2**, 7850–7860 (2019).
35. David, T. M., Dev, P. R., Wilson, P., Sagayaraj, P. & Mathews, T. A critical review on the variations in anodization parameters toward microstructural formation of $TiO_2$ nanotubes. *Electrochemical Science Advances* **2**, (2022).
36. Eissa, D. S., El-Hagar, S. S., Ashour, E. A. & Allam, N. K. Electrochemical nano-patterning of brass for stable and visible light-induced photoelectrochemical water splitting. *Int J Hydrogen Energy* **44**, 14588–14595 (2019).
37. Dezfoolian, M., Rashchi, F. & Nekouei, R. K. Synthesis of copper and zinc oxides nanostructures by brass anodization in alkaline media. *Surf Coat Technol* **275**, 245–251 (2015).
38. Ryczek, K. *et al.* Fast fabrication of nanostructured semiconducting oxides by

anodic oxidation of brass. *Mater Sci Semicond Process* **113**, 105035 (2020).
39. Bahnasawy, N., Elbanna, A. M., Ramadan, M. & Allam, N. K. Fabrication of polyhedral Cu–Zn oxide nanoparticles by dealloying and anodic oxidation of German silver alloy for photoelectrochemical water splitting. *Sci Rep* **12**, 16785 (2022).
40. Imazeki, Y. *et al.* Band Alignment at n-GaN/Electrolyte Interface Explored by Photo-Induced Offset of Open-Circuit Potential for Efficient Water Splitting. *ECS Trans* **77**, 25–30 (2017).
41. Chen, Z., Dinh, H. N. & Miller, E. *Photoelectrochemical Water Splitting*. (Springer New York, 2013). doi:10.1007/978-1-4614-8298-7.
42. Elgrishi, N. *et al.* A Practical Beginner's Guide to Cyclic Voltammetry. *J Chem Educ* **95**, 197–206 (2018).
43. Sanad, M. F. *et al.* Co–Cu Bimetallic Metal Organic Framework Catalyst Outperforms the Pt/C Benchmark for Oxygen Reduction. *J Am Chem Soc* **143**, 4064–4073 (2021).
44. Hong, H. L., Wang, Q., Dong, C. & Liaw, P. K. Understanding the Cu-Zn brass alloys using a short-range-order cluster model: significance of specific compositions of industrial alloys. *Sci Rep* **4**, 7065–7069 (2014).
45. Cretu, V. *et al.* Synthesis, characterization and DFT studies of zinc-doped copper oxide nanocrystals for gas sensing applications. *J Mater Chem A Mater* **4**, 6527–6539 (2016).
46. Zoolfakar, A. S., Rani, R. A., Morfa, A. J., O'Mullane, A. P. & Kalantar-Zadeh, K. Nanostructured copper oxide semiconductors: A perspective on materials, synthesis methods and applications. *J Mater Chem C Mater* **2**, 5247–5270 (2014).
47. Sander, T. *et al.* Correlation of intrinsic point defects and the Raman modes of cuprous oxide. *Phys Rev B Condens Matter Mater Phys* **90**, (2014).
48. Dhonge, B. P., Ray, S. S. & Mwakikunga, B. Electronic to protonic conduction switching in Cu2O nanostructured porous films: The effect of humidity exposure. *RSC Adv* **7**, 21703–21712 (2017).
49. Sivalingam, M. M. *et al.* Copper Oxide Nanorod/Reduced Graphene Oxide Composites for $NH_3$ Sensing. *ACS Appl Nano Mater* **4**, 12977–12985 (2021).
50. Karthikeyan, B. Raman spectral probed electron–phonon coupling and phonon lifetime properties of Ni-doped CuO nanoparticles. *Appl Phys A Mater Sci Process* **127**, (2021).
51. Ahmed, N., Ramadan, M., El Rouby, W. M. A., Farghali, A. A. & Allam, N. K. Non-precious co-catalysts boost the performance of TiO2 hierarchical hollow mesoporous spheres in solar fuel cells. *Int J Hydrogen Energy* **43**, 21219–21230 (2018).
52. Zhang, Z. & Wang, P. Highly stable copper oxide composite as an effective photocathode for water splitting via a facile electrochemical synthesis strategy. *J. Mater. Chem.* **22**, 2456–2464 (2012).
53. Badawy, I. M., Ismail, A. M., Khedr, G. E., Taha, M. M. & Allam, N. K. Selective electrochemical reduction of CO2 on compositionally variant bimetallic Cu–Zn electrocatalysts derived from scrap brass alloys. *Sci Rep* **12**, 13456 (2022).
54. Maroie, S., Caudano, R. & Verbist, J. The oxidation of the α and β phases of brass studied by XPS and nuclear reaction spectroscopy. *Surf Sci* **100**, 1–13 (1980).
55. VANHERWIJNEN, T. Brass formation in a copper/zinc oxide CO shift catalyst. *J*

*Catal* **34**, 209–214 (1974).
56. Dhineshbabu, N. R., Rajendran, V., Nithyavathy, N. & Vetumperumal, R. Study of structural and optical properties of cupric oxide nanoparticles. *Appl Nanosci* **6**, 933–939 (2016).
57. Hasan, M. M., Khedr, G. E. & Allam, N. K. Nanospheres/Ni Foam as High-Performance Heterostructured Electrocatalysts for Hydrogen Evolution Reaction: Unveiling the Interfacial Interaction. *ACS Appl Nano Mater* **5**, 15457–15464 (2022).
58. Fang, M., Dong, G., Wei, R. & Ho, J. C. Hierarchical Nanostructures: Design for Sustainable Water Splitting. *Adv Energy Mater* **7**, 1700559 (2017).
59. Patel, P. P. *et al.* Electrochemically active and robust cobalt doped copper phosphosulfide electro-catalysts for hydrogen evolution reaction in electrolytic and photoelectrochemical water splitting. *Int J Hydrogen Energy* **43**, 7855–7871 (2018).
60. Sun, H. *et al.* Molecular Engineering of Conjugated Acetylenic Polymers for Efficient Cocatalyst-free Photoelectrochemical Water Reduction. *Angewandte Chemie International Edition* **58**, 10368–10374 (2019).
61. Su, J., Liu, C., Liu, D., Li, M. & Zhou, J. Enhanced Photoelectrochemical Performance of the BiVO4/Zn:BiVO4 Homojunction for Water Oxidation. *ChemCatChem* **8**, 3279–3286 (2016).
62. Day, C. *et al.* Utilizing Cyclic Voltammetry to Understand the Energy Storage Mechanisms for Copper Oxide and its Graphene Oxide Hybrids as Lithium-Ion Battery Anodes. doi:10.1002/cssc.v13.6.
63. Peter, L. M., Walker, A. B., Bein, T., Hufnagel, A. G. & Kondofersky, I. Interpretation of photocurrent transients at semiconductor electrodes: Effects of band-edge unpinning. *Journal of Electroanalytical Chemistry* **872**, 114234 (2020).
64. Santos, H. L. S., Corradini, P. G., Andrade, M. A. S. & Mascaro, L. H. CuO/NiOx thin film–based photocathodes for photoelectrochemical water splitting. *Journal of Solid State Electrochemistry* **24**, 1899–1908 (2020).
65. Amer, A. W., El-Sayed, M. A. & Allam, N. K. Tuning the Photoactivity of Zirconia Nanotubes-Based Photoanodes via Ultrathin Layers of ZrN: An Effective Approach toward Visible-Light Water Splitting. *Journal of Physical Chemistry C* **120**, 7025–7032 (2016).
66. Sivula, K. *et al.* Photoelectrochemical Water Splitting with Mesoporous Hematite Prepared by a Solution-Based Colloidal Approach. *J Am Chem Soc* **132**, 7436–7444 (2010).
67. Tapia, C. *et al.* Achieving visible light-driven hydrogen evolution at positive bias with a hybrid copper–iron oxide|$TiO_2$-cobaloxime photocathode. *Green Chemistry* **22**, 3141–3149 (2020).
68. Shi, W. *et al.* Carbon coated Cu2O nanowires for photo-electrochemical water splitting with enhanced activity. *Appl Surf Sci* **358**, 404–411 (2015).
69. Tan, R., Hwang, S. W., Sivanantham, A. & Cho, I. S. Solution synthesis and activation of spinel CuAl2O4 film for solar water-splitting. *J Catal* **400**, 218–227 (2021).
70. Kampmann, J. *et al.* How photocorrosion can trick you: a detailed study on low-bandgap Li doped CuO photocathodes for solar hydrogen production. *Nanoscale* **12**, 7766–7775 (2020).